

Envelope structure of deeply embedded young stellar objects in the Serpens Molecular Cloud

Michiel R. Hogerheijde¹, Ewine F. van Dishoeck, and Jante M. Salverda²,
 Sterrewacht Leiden, P.O. Box 9513, 2300 RA, Leiden, The Netherlands

and

Geoffrey A. Blake

Division of Geological and Planetary Sciences, California Institute of Technology, MS 150-21,
 Pasadena, CA 91125

ABSTRACT

Aperture-synthesis and single-dish (sub) millimeter molecular-line and continuum observations reveal in great detail the envelope structure of deeply embedded young stellar objects (SMM 1 = FIRS 1, SMM 2, SMM 3, SMM 4) in the densely star-forming Serpens Molecular Cloud. SMM 1, 3, and 4 show partially resolved ($> 2'' = 800$ AU) continuum emission in the beam of the Owens Valley Millimeter Array at $\lambda = 3.4\text{--}1.4$ mm. The continuum visibilities accurately constrain the density structure in the envelopes, which can be described by a radial power law with slope -2.0 ± 0.5 on scales of 300 AU to 8000 AU. Inferred envelope masses within a radius of 8000 AU are 8.7, 3.0, and $5.3 M_\odot$ for SMM 1, 3, and 4, respectively. A point source with 20%–30% of the total flux at 1.1 mm is required to fit the observations on long baselines, corresponding to warm envelope material within ~ 100 AU or a circumstellar disk. No continuum emission is detected interferometrically toward SMM 2, corresponding to an upper limit of $0.2 M_\odot$ assuming $T_d = 24$ K. The lack of any compact dust emission suggests that the SMM 2 core does not contain a central protostar.

Aperture-synthesis observations of the ^{13}CO , C^{18}O , HCO^+ , H^{13}CO^+ , HCN , H^{13}CN , N_2H^+ 1–0, SiO 2–1, and SO 2₂–1₁ transitions reveal compact emission toward SMM 1, 3, and 4. SMM 2 shows only a number of clumps scattered throughout the primary field of view, supporting the conclusion that this core does not contain a central star. The compact molecular emission around SMM 1, 3, and 4 traces 5''–10'' (2000–4000 AU) diameter cores that correspond to the densest regions of the envelopes, as well as material directly associated with the molecular outflow. Especially prominent are the optically thick HCN and HCO^+ lines which show up brightly along the walls of the outflow cavities. SO and SiO trace shocked material, where their abundances may be enhanced by 1–2 orders of magnitude over dark-cloud values.

¹Currently at: Astronomy Department, University of California at Berkeley

²Currently at: Department of Physics and Astronomy, Vrije Universiteit, Amsterdam, The Netherlands

A total of 31 molecular transitions have been observed with the James Clerk Maxwell and Caltech Submillimeter telescopes in the 230, 345, 490, and 690 GHz atmospheric windows toward all four sources, containing, among others, lines of CO, HCO^+ , HCN, H_2CO , SiO, SO, and their isotopomers. These lines show $20\text{--}30\text{ km s}^{-1}$ wide line wings, deep and narrow ($1\text{--}2\text{ km s}^{-1}$) self-absorption, and $2\text{--}3\text{ km s}^{-1}$ FWHM line cores. The presence of highly excited lines like ^{12}CO 4–3 and 6–5, ^{13}CO 6–5, and several H_2CO transitions indicates the presence of material with temperatures $\gtrsim 100\text{ K}$. Monte-Carlo calculations of the molecular excitation and line transfer show that the envelope model derived from the dust emission can successfully reproduce the observed line intensities. The depletion of CO in the cold gas is modest compared to values inferred in objects like NGC 1333 IRAS 4, suggesting that the phase of large depletions through the entire envelope is short-lived and may be influenced by the local star-formation density. Emission in high excitation lines of CO and H_2CO requires the presence of a small amount of $\sim 100\text{ K}$ material, comprising less than 1% of the total envelope mass and probably associated with the outflow or the innermost region of the envelope. The derived molecular abundances in the warm ($T_{\text{kin}} > 20\text{ K}$) envelope are similar to those found toward other class 0 YSOs like IRAS 16293–2422, though some species appear enhanced toward SMM 1. Taken together, the presented observations and analysis provide the first comprehensive view of the physical and chemical structure of the envelopes of deeply embedded young stellar objects in a clustered environment on scales between 1000 and 10,000 AU.

Subject headings: ISM: molecules — stars: formation — stars: low mass, brown dwarfs — stars: pre-main sequence

1. Introduction

The earliest stages of star formation are represented by deeply embedded, class 0 young stellar objects (YSOs; André, Ward-Thompson, & Barsony 1993). These sources have spectral energy distributions (SEDs) which are well fit by a single black body curve of $T_{\text{eff}} \lesssim 30\text{ K}$, are undetected at wavelengths shorter than $\sim 10\text{ }\mu\text{m}$, and still have most of their mass in a circumstellar envelope. Thus, class 0 sources are ideal objects to investigate the physical and chemical conditions during the earliest phases of the star-forming process, to test theoretical models of cloud core collapse (e.g., Shu 1977; Terebey, Shu, & Cassen 1984; Fiedler & Mouschovias 1992; Boss 1993), and to study the influence of the bipolar outflow on the structure and chemistry of the envelope. This paper presents single-dish and aperture synthesis observations of dust and molecular lines of four class 0 candidates in the Serpens Molecular Cloud, tracing the structure and chemistry of their envelopes on 1000–10,000 AU scales ($3''\text{--}30''$). These data have higher spatial resolution than previous studies, and show a detailed picture of the structure and chemistry of both the inner and

outer regions of the envelopes.

Previous dust continuum and molecular line observations of the envelopes of class 0 YSOs used mostly single-dish telescopes (e.g., NGC 1333 IRAS 4A and 4B, Blake et al. 1995; IRAS 16293–2422, Walker, Carlstrom, & Bieging 1993; Blake et al. 1994, van Dishoeck et al. 1995). These observations show that the outer envelopes are dense, with $n_{\text{H}_2} \approx 10^6\text{--}10^7 \text{ cm}^{-3}$, and cold, at $T_d \approx 30 \text{ K}$, and that the molecular abundances in some objects may be significantly depleted by freezing out onto dust grains (e.g., Blake et al. 1995; see also Mundy & McMullin 1997). Surveys in HCO^+ (Gregersen et al. 1997), and in H_2CO , CS, and N_2H^+ (Mardones et al. 1997) indicate that line-profile asymmetries predicted for infalling envelopes are more readily observed during the deeply embedded class 0 phase than toward more evolved class I objects. Also, class 0 YSOs are often found to drive highly collimated outflows (e.g., André et al. 1990; Guilloteau et al. 1992; Zhang et al. 1995; Blake et al. 1995; Gueth et al. 1997). These outflows affect the structure of the molecular envelope, as well as its chemistry. In material heated by the outflow to 60 K or more, molecules are released from the grain surfaces into the gas phase, and shocks can destroy dust particles (e.g., van Dishoeck et al. 1995; Blake et al. 1995; Bachiller & Pérez Gutiérrez 1997). Several important questions about the envelopes around class 0 sources are unanswered. How does their density structure compare to theoretical models of protostellar collapse? Is the structure different in clustered regions compared with isolated objects? To what extent is their structure and chemistry influenced by the outflow? How strongly are molecular abundances depleted in the cold, dense regions?

The Serpens Molecular Cloud provides a particularly good opportunity to study several deeply embedded class 0 objects originating from the same molecular cloud. Casali, Eiroa, & Duncan (1993) have detected four submillimeter continuum sources without any near-infrared counterparts (SMM 1, 2, 3, and 4). Most previous studies of these objects have been performed with single-dish telescopes at $\sim 15''$ resolution (e.g., White et al. 1995; Hurt et al. 1996b). This paper presents single-dish and aperture-synthesis observations of molecular lines and dust continuum at (sub) millimeter wavelengths toward SMM 1, 2, 3, and 4, with spatial resolutions between $1''$ and $20''$ ($\sim 400\text{--}8000 \text{ AU}$). The protostellar nature of three sources, SMM 1, 3, and 4, is confirmed on the basis of the interferometer results, while SMM 2 appears to be a warm cloud condensation without any central source. The continuum observations allow a determination of the density and temperature structure of the envelopes surrounding SMM 1, 3, and 4. The molecular line data can be explained by this same envelope model, but require that $\lesssim 1\%$ of the gas has a much higher temperature of $\sim 100 \text{ K}$. The aperture-synthesis observations trace $5''\text{--}10''$ (2000–4000 AU) cores around the YSOs, as well as the interaction of the outflow with surrounding material. This study of a group of deeply embedded YSOs has the spatial resolution required to directly sample the protostellar envelopes in a clustered environment. The Serpens results will be compared to class 0 objects in other clouds, as well as to a set of more evolved class I sources studied in emission of the same molecular transitions by Hogerheijde et al. (1997, 1998).

The outline of the paper is as follows. Section 2 introduces the characteristics of the Serpens

Molecular Cloud and its embedded YSOs. After presenting the observations in §3, we discuss the results of the continuum measurements in §4.1, and construct an envelope model in §4.2. Section 5 analyzes in detail the molecular line emission observed in the interferometer (§5.1) and single-dish beams (§5.2) toward the individual sources. In §5.3 the molecular line emission is compared to model predictions based on the envelope structure derived from the dust continuum. The results are further discussed and compared to other class 0 and class I YSOs in §6. Finally, §7 summarizes the main findings of the paper.

2. The Serpens Molecular Cloud and its embedded protostars

The Serpens Molecular Cloud appears to be forming a loosely bound cluster of low- to intermediate-mass stars. Eiroa & Casali (1992) have identified 51 near-infrared sources as T Tauri stars (see also Giovannetti et al. 1998). Nordh et al. (1982) and Harvey et al. (1984) first identified SMM 1, also called FIRS 1, as a deeply embedded YSO. Subsequent submillimeter continuum maps by Casali et al. (1993) resulted in the detection of four strong sources without near-infrared counterparts, SMM 1–4. Recently, Testi & Sargent (1998) carried out an extensive survey of the Serpens cloud with the Owens Valley Millimeter Array in CS 2–1 and 3 mm continuum, identifying 32 cores with masses in the range of $0.4\text{--}16 M_{\odot}$. The SMM 1–4 sources stand out as the brightest of these cores, and represent a second, more recent phase of star formation in the Serpens cloud compared to the near-infrared sources. Their spectral energy distributions are well fit by single blackbodies with temperatures of 20–27 K, characteristic of class 0 YSOs (Hurt & Barsony 1996a). Observations of ^{12}CO , HCO^+ , and H_2CO lines indicate the presence of warm ($T_{\text{kin}} = 40\text{--}190$ K) and dense ($n_{\text{H}_2} \approx 2 \times 10^6 \text{ cm}^{-3}$) gas associated with bipolar outflows, as evidenced by broad line wings (White, Casali, & Eiroa 1995; Hurt, Barsony, & Wootten 1996b).

Near-infrared observations also reveal evidence for outflows. Herbst, Beckwith, & Robberto (1997) detected a number of H_2 knots, possibly a jet, emanating from SMM 3, whereas Eiroa et al. (1997) report the detection of a similar string of H_2 knots possibly associated with SMM 4. SMM1 shows several signs of energetic activity, such as H_2O maser emission (Dinger & Dickinson 1980; Rodríguez et al. 1980) and near-infrared H_2 emission (Eiroa & Casali 1989). At cm wavelengths, the source is triple, with two diametrically opposed lobes moving away at $\sim 200 \text{ km s}^{-1}$ from the central source. McMullin et al. (1994) performed an interferometric and single-dish study of the northwestern part of the Serpens Molecular Cloud including SMM 1 and the condensation S68 N, $2'$ north of SMM 1, using lines of CS, CH_3OH , and other molecules. They find that most of the $70 M_{\odot}$ in this region is distributed on extended scales, indicative of a young age of the sources, with $\sim 10 M_{\odot}$ in a circumstellar component around SMM 1. They infer abundances for CO and HCO^+ corresponding to those found in dark clouds, while CS, HCN, and H_2CO may be mildly depleted. Evidence for freezing out of molecules on grains is also provided by direct observations of solid CO in the Serpens Molecular Cloud by Chiar et al. (1994).

The distance to the Serpens cloud core has been the subject of much debate. De Lara,

Chavarria-K, & López-Molina (1991) derive a value of 310 ± 40 pc, based on extinction measurement of five stars. Chiar (1996) finds 425 ± 45 pc based on seven stars, including new observations of the five stars used by de Lara et al., all of which indicate a larger distance. One of these stars, R16, has a derived distance of 628 pc, but is included by Chiar because its image on the POSS plate suggests it is an embedded object associated with the Serpens cloud. Excluding this star lowers the distance estimate to 390 pc. Here we will adopt 400 pc as a fiducial estimate of the distance to Serpens. Bolometric luminosities and other quantities taken from the literature are scaled to the adopted distance.

3. Observations

Table 1 lists the coordinates of SMM 1, 2, 3, and 4, together with their bolometric luminosity scaled to a distance of 400 pc, continuum flux at $\lambda = 1.1$ mm, and estimates of the stellar mass. The coordinates are derived from the interferometric continuum emission, and differ by up to $5''$ from those quoted by Casali et al. (1993) for SMM 3 and 4. Lower limits to the stellar masses follow from the assumption that all luminosity is due to accretion at a rate of $10^{-5} M_\odot \text{ yr}^{-1}$, while upper limits are the stellar masses which produce the same luminosity on the zero-age main sequence. Table 2 gives an overview of the data presented in this paper. The following subsections present the details of the interferometer and single-dish observations.

3.1. Millimeter-interferometer observations

Observations of the transitions listed in Table 2 were obtained with the six-element Owens Valley Radio Observatory (OVRO) Millimeter Array³ between 1994 and 1997, simultaneously with the continuum emission over a 1 GHz bandwidth at $\lambda = 3.4, 3.2, 2.7$, and 1.4 mm. Data taken in the low-resolution and equatorial configurations were combined, resulting in a u - v coverage with spacings between 3 and 60–80 $k\lambda$ at 3.4–2.7 mm for the observed lines and continuum, and between 10 and 100–180 $k\lambda$ at 1.4 mm in continuum only. This corresponds to naturally weighted, synthesized beams of $3''$ – $5''$ and $1''$ FWHM, respectively. Spectral line data were recorded in two 64-channel bands with respective widths of 2 and 8 MHz, resulting in velocity resolutions of ~ 0.1 and $\sim 0.4 \text{ km s}^{-1}$. The visibility data were calibrated using the MMA package, developed specifically for OVRO (Scoville et al. 1993). The quasar PKS 1749+096 served as phase calibrator; the amplitudes were calibrated on 3C 454.3, 3C 273, or Neptune. The correlator passbands are calibrated using noise tube integrations and observations of 3C 454.3 and 3C 273.

The interferometer data were edited in the usual manner by flagging a small number of data

³The Owens Valley Millimeter Array is operated by the California Institute of Technology under funding from the U.S. National Science Foundation (#AST96-13717).

points with clearly deviating amplitudes and phases. The quality of the continuum data at 3.4–2.7 mm allowed self-calibration of the visibility phases, which was subsequently applied to the line data, decreasing the noise level by a small amount. Natural weighting was used to clean the data. The interferometer dirty beam has strong N–S side lobes because of the $+1^\circ$ declination of Serpens. In many cases the position of the initial clean-components had to be constrained to a $\sim 20''$ box around the source position to ensure proper deconvolution. An additional complication for cleaning of the molecular-line data toward SMM 3 was the presence of strong emission from SMM 4 approximately one primary beam ($\sim 70''$) to the south. Care had to be taken to prevent any emission from SMM 4 appearing within the primary field of view around SMM 3.

The reduced continuum data have RMS noise levels of 2–6 mJy beam $^{-1}$ at 3.4–2.7 mm and 30 mJy beam $^{-1}$ at 1.4 mm. For the molecular line data the typical noise is 0.1–0.2 Jy beam $^{-1}$ per 125 kHz channel. Reduction and analysis of the visibility data were carried out within the MIRIAD software package.

3.2. Single-dish observations

The single-dish line observations between 219 and 690 GHz were obtained between 1995 March and 1996 August with the James Clerk Maxwell Telescope (JCMT)⁴ and the Caltech Submillimeter Observatory (CSO)⁵. The observed transitions are listed in Table 2. The single-dish observations were reduced and analyzed with the CLASS software package.

The JCMT observations at 230, 345, and 490 GHz were obtained with FWHM beam sizes of 19'', 14'', and 10'', respectively. The observations were made using a position-switch of typically 15''–60', ensuring emission-free offset positions. Pointing accuracy is estimated to be $\sim 5''$. As indicated in Table 2, maps covering regions between $20'' \times 20''$ and $40'' \times 40''$ around the sources were taken in a number of lines, sampled at $\frac{1}{2}$ – $\frac{2}{3}$ beam sizes. In HCO $^+$ 3–2, fully sampled maps were obtained *on-the-fly*. The spectra were recorded with the Digital Autocorrelation Spectrometer, with typical velocity resolutions of 0.05–0.1 km s $^{-1}$. The H₂CO 3₀₃–2₀₂ and 3₂₂–2₂₁ spectra were observed in a single frequency setting over a total bandwidth of 500 MHz and at a resolution of 0.9 km s $^{-1}$, also covering the HC₃N 24–23, C₃H₂ 5₂₄–4₁₃, CH₃OH 4₂–3₁ E, and SO 5₅–4₄ lines. The data were converted to the main-beam antenna temperature scale using $\eta_{\text{mb}} = 0.69$ (230 GHz), 0.58 (345 GHz), and 0.53 (490 GHz), obtained by the JCMT staff from measurements of the planets. Typical RMS noise levels are 0.1–0.3 K in 0.15 km s $^{-1}$ wide channels.

⁴The James Clerk Maxwell Telescope is operated by the Joint Astronomy Centre, on behalf of the Particle Physics and Astronomy Research Council of the United Kingdom, the Netherlands Organization for Scientific Research and the National Research Council of Canada.

⁵The Caltech Submillimeter Observatory is operated by the California Institute of Technology under funding from the U.S. National Science Foundation (#AST96-15025).

Using the CSO, observations were obtained of ^{12}CO and ^{13}CO 6–5 with a FWHM beam size of $10''$, and of H^{13}CO^+ 4–3 at $22''$, the latter of which also contains the SO 88-77 line. The observations were made using a position switch of $15'$ for the ^{12}CO and ^{13}CO spectra, and a beam switch of $180''$ for the H^{13}CO^+ data, ensuring emission-free offset positions. Pointing was checked regularly, and found to vary by up to $5''$. At the frequency of the ^{12}CO and ^{13}CO 6–5 lines (660–690 GHz), an additional source of positional error was the correction for the atmospheric refraction, which is comparable to the FWHM beam size ($\sim 10''$). It is estimated that the pointing at these frequencies is no better than $\sim 10''$. Five-point maps with $10''$ spacing were obtained for ^{12}CO and ^{13}CO 6–5. The spectral lines were recorded with the facility 50 MHz and 500 MHz bandwidth Acousto–Optical Spectrometers (AOSSs). The spectra were converted to the main-beam antenna scale using $\eta_{\text{mb}} = 0.44$ (^{12}CO , ^{13}CO) and 0.65 (H^{13}CO^+ , SO), obtained from measurements of Jupiter. Resulting RMS noise levels are 0.6 K per 0.5 km s^{-1} channel for ^{12}CO and ^{13}CO , and 0.1 K per 0.15 km s^{-1} for H^{13}CO^+ and SO.

4. Dust continuum emission

4.1. Interferometer results

Continuum emission at $\lambda = 3.4$, 3.2 , 2.7 , and 1.4 mm is readily detected by OVRO toward SMM 1, 3, and 4. Peak intensities and integrated fluxes are listed in Table 3. No continuum emission is detected toward SMM 2 with an upper limit of ~ 5 mJy at 3.4 mm. Figure 1 shows the naturally weighted, cleaned continuum images. The emission is mostly unresolved and symmetric about the source position. Table 1 lists the best-fit source positions for SMM 1, 3, and 4. Our observations, which have higher spatial resolution and positional accuracy than do the JCMT continuum maps of Casali et al. (1993), yield positions for SMM 3 and SMM 4 nearly $5''$ west of those listed by these authors. We will adopt our best-fit coordinates as their true positions. The best-fit coordinates of SMM 1 agree with the radio position from Rodríguez et al. (1989) to within the accuracy of the measurements. Its emission at cm wavelengths, and the expected flat spectral index for non-thermal radiation, indicates that $> 95\%$ of the emission of SMM 1 at 3.4–1.4 mm is due to thermal emission from dust (Rodríguez et al. 1989; McMullin et al. 1994).

Figure 2 shows the vector-averaged visibility amplitudes as functions of projected baseline length for the observed sources and wavelengths, averaged in 5 – 10 $\text{k}\lambda$ wide bins. These plots essentially give the Fourier transform of the symmetric part of the sky brightness about the source center. A point source has a flux independent of baseline length, while the flux of an extended source decreases with increasing u - v separation. The observations show both extended and unresolved ($< 2'' = 800$ AU) emission towards SMM 1, 3, and 4. The extended emission traces the envelopes surrounding the YSOs, and the steep decrease of flux with u - v distance suggests a radial power-law distribution for the density. A Gaussian distribution, for example, would appear Gaussian as well in a plot of this type. The unresolved emission may contain contributions from

the dense central regions of the power-law envelope as well as that from a circumstellar disk. The amplitudes on baselines $\gtrsim 60$ $k\lambda$ at the different wavelengths indicate a spectral index of 2.0 for the unresolved emission, consistent with optically thick, thermal emission.

4.2. A model for the continuum emission

The high signal-to-noise of the resolved continuum emission in the interferometer beam, together with the single-dish (sub) millimeter and IRAS fluxes of Casali et al. (1993) and Hurt & Barsony (1996a), provides constraints on the mass and density distribution of the envelopes. Our modeling explicitly includes sampling at the discrete (u, v) positions of the visibility data and the resulting resolving-out of extended emission.

Table 4 summarizes the basic parameters of the adopted envelope model. For the density distribution we assume a radial power law, $\rho \propto r^{-p}$, as suggested by the visibility amplitudes of Fig. 2. The index p is a free parameter of the model, and is varied between 1 and 3. Theoretical models for cloud core collapse predict slopes between -1 and -2 (e.g., Shu 1977; Lizano & Shu 1989). Values for the dust emissivity at millimeter wavelengths are taken from Ossenkopf & Henning (1994), which include dust coagulation in a medium of 10^6 H_2 cm^{-3} and thin ice mantles, with $\kappa_\nu(1.3\text{ mm}) = 0.9\text{ cm}^2\text{ g}^{-1}$ (dust) and $\kappa_\nu \propto \nu^{1.5}$. Inner and outer radii of 100 and 8000 AU are adopted, the exact values of which do not influence the derived parameters significantly.

The dust temperature is approximated by a power law of index -0.4 , expected for a centrally heated, spherical cloud which is optically thin to the bulk of the radiation (cf. Rowan-Robinson 1980; Adams & Shu 1987). At large radii the temperature is not allowed to drop below 8 K, corresponding to the typical value maintained through cosmic ray heating of the hydrogen gas. To fit the peak of the SED at 50–100 μm , dust temperatures at 1000 AU of 27 K (SMM 1), 24 K (SMM 3), and 20 K (SMM 4) are required, similar to the values found by Hurt & Barsony (1996a). The latter authors assume a single dust temperature, but our derived temperature gradient is sufficiently shallow to give similar results. A self-consistent calculation of the heating and cooling balance of the dust for representative envelope parameters confirms that the temperature follows $T_d \propto r^{-0.4}$ outside radii of 200–400 AU (see van der Tak et al. 1998 for details of the temperature calculations). Toward smaller radii, the temperature increases more rapidly. Since these radii are not resolved in the interferometer observations, the associated excess emission is fitted by a simple point source instead, with spectral index $\alpha = 2.0$ (cf. §4.1).

The resulting model has three free parameters. The total envelope mass M_{env} within a radius of 8000 AU is found from the single-dish 1.1 mm continuum fluxes observed in the 18'' JCMT beam (Casali et al. 1993). The flux of the unresolved point source follows from the flux on long baselines, and the density power-law index p is constrained from the change of the visibility amplitude with $u-v$ separation. Figure 3 illustrates this for models fitted to the total 1.1 mm flux with various power-law indices and point-source fluxes. Models with a shallower density distribution have

amplitudes which decrease faster with increasing u - v distance. The best correspondence to the observed amplitudes of SMM 1 is found for $p = 2.0 \pm 0.5$, which accurately fits the flux increase toward smaller u - v distances, and a point-source flux of 0.13 Jy at 2.7 mm.

Similar best-fit results with $p = 2.0 \pm 0.5$ are found for SMM 3 and 4 with point-source fluxes at 2.7 mm of 0.05 Jy and 0.07 Jy, respectively. The corresponding curves are drawn in Fig. 2 for all sources. The inferred slopes of -2.0 for the density agree well with theoretical predictions for very young sources (e.g., Shu 1977). While the model curves provide very good fits to the 3.4–2.7 mm fluxes, they do underestimate the large scale emission at 1.4 mm. Part of this discrepancy may be explained by a steeper frequency dependency of the dust emissivity than the $\sim \nu^{1.5}$ of the adopted model (Ossenkopf & Henning 1994). It may also indicate that warm material is distributed over larger scales than assumed in the model, in which it is confined to the inner few hundred AU.

Corresponding envelope masses are $8.7 M_{\odot}$ for SMM 1, $3.0 M_{\odot}$ for SMM 3, and $5.3 M_{\odot}$ for SMM 4. These values depend on the adopted dust emissivity of Ossenkopf & Henning (1994), which is uncertain by approximately a factor of 2–3 (cf. also Agladze et al. 1994; Pollack et al. 1994). These masses exceed the limits placed on the stellar mass of 0.7 – $3.9 M_{\odot}$ (SMM 1), 0.1 – 2.2 (SMM 3), and 0.1 – $2.3 M_{\odot}$ (SMM 4; Table 1), confirming the young age of these sources and their classification as class 0 YSOs.

The point-source fluxes correspond to masses within 100 AU of 0.9, 0.4, and $0.5 M_{\odot}$ for SMM 1, SMM 3, and SMM 4, respectively, adopting a dust temperature of 100 K and optically thin radiation. However, the self-consistent temperature calculations suggest that the temperature exceeds 100 K by factors of a few on these small radii, while the spectral indices of the point-source emission indicate that the emission is optically thick at millimeter wavelengths. These considerations make the estimated masses within 100 AU uncertain by at least a factor of a few. A small fraction of the unresolved emission may originate in a circumstellar disk, but observations at much higher angular resolution are required to separate this from emission due to the inner envelope. Using single-baseline interferometry, Pudritz et al. (1996) infer a flux of 0.12 Jy at $\lambda = 1.4$ mm for a disk around the class 0 YSO VLA 1623 ($d = 160$ pc). Scaling to the distance of Serpens and to $\lambda = 2.7$ mm using a spectral index of 2.0, this corresponds to only 5 mJy, suggesting that the fitted point-source emission of 50–130 mJy toward these sources is dominated by compact envelope material. Calvet, Hartmann, & Strom (1997) infer the presence of hot dust very close to the star (~ 0.1 AU) as an explanation for the weakness of CO $v = 2$ – 0 emission and absorption from Class I objects through veiling by infalling dust from the envelope.

5. Molecular line emission

The dust continuum observations provide direct constraints on the density gradient in the envelope. Molecular-line data offer a complementary view of the density structure, and probe the influence of the outflow on the envelope and the response of the chemistry. The various

components in the protostellar environment traced by the observations are summarized in Table 5.

5.1. Interferometer results

Compact emission is detected in most transitions observed toward the four sources. Figure 4 shows the naturally weighted, cleaned images of the integrated intensity; Fig. 5 presents the spectra obtained within a $5'' \times 5''$ box around the image maximum, corresponding approximately to the synthesized beam. Table 6 lists the velocity-integrated brightness temperatures $\int T_b dV$ averaged over $5'' \times 5''$ and $20'' \times 20''$ regions around the source positions listed in Table 1. Estimates of the opacity averaged over the line profiles follow from the observed ratios of $\text{C}^{18}\text{O}/^{13}\text{CO}$, $\text{H}^{13}\text{CO}^+/\text{HCO}^+$, and $\text{H}^{13}\text{CN}/\text{HCN}$, and the relative intensities of the hyperfine components of HCN and N_2H^+ . Isotopic abundance ratios of $[^{13}\text{CO}]:[\text{C}^{18}\text{O}] = 8:1$ and $[\text{HCO}^+]:[\text{H}^{13}\text{CO}^+] = [\text{HCN}]:[\text{H}^{13}\text{CN}] = 65:1$ are assumed (Wilson & Rood 1994).

Extended ($\gtrsim 20''$) emission from optically thick material is resolved out by the interferometer in ^{13}CO , HCO^+ , and HCN 1–0 toward all sources. This results in apparent, deep absorption features in the spectra of Fig. 5, and negative intensities in the images of Fig. 4. The level of resolved-out ^{13}CO 1–0 emission toward SMM 4 is so large that no positive signal is left in the integrated-intensity image. Using only the velocity interval of $4\text{--}8 \text{ km s}^{-1}$, where positive emission is detected, yields a core of $\sim 10''$ diameter around the source. Keeping in mind these high levels of resolved-out emission, the interferometer molecular line data can be interpreted, with caution, both qualitatively and quantitatively (cf. also §5.3).

As discussed in §3.1, the pointing centers of the observations of SMM 2, 3, and 4 are separated by only one primary-beam size, and care had to be taken to prevent emission spilling over in the deconvolved images. Figure 4 presents the cleaned images at the different transitions in single panels containing all three sources. The plotted images have been cleaned individually, since no reliable mosaic could be obtained with the pointing centers separated by a full primary beam. Maximum entropy deconvolution of the mosaicked images did yield consistent results, however.

Estimates of the molecular abundances on the scales traced by the interferometer are derived in §5.3 using detailed modeling of the molecular excitation, radiative transfer, and (u, v) sampling. Detailed analysis has shown that the derived abundances may be in error by as much as a factor of 5 if the intensities listed in Table 6 are used without going through this careful procedure (Hogerheijde 1998; Hogerheijde & van der Tak 1998).

The following sections discuss the specific details of the aperture-synthesis results for the individual sources. In summary, the C^{18}O , ^{13}CO , and H^{13}CO^+ lines probe $5''\text{--}10''$ (2000–4000 AU) cores surrounding SMM 1, 3, and 4. The optically thick HCO^+ and HCN emission is associated with the walls of the outflow cavities, while SiO and SO probably reveal shocked material where the outflow impacts directly on the envelope. These physical components are similar to those inferred toward other embedded YSOs (e.g., B5 IRS 1, Langer, Velusamy, & Xie 1996; B1, Hirano

et al. 1997; and class I YSOs in Taurus, Hogerheijde et al. 1997). None of the four sources shows detectable emission in C^{34}S , while in C_3H_2 only a number of scattered clumps are detected toward SMM 1 and 4. The latter line probably traces dense condensations in the surrounding, quiescent cloud, and is not further considered here. The 3σ upper limit of 3.9 K km s^{-1} on the emission of C^{34}S toward SMM 1 is consistent with the weak detection of CS 2–1 toward this source of $\sim 6 \text{ K km s}^{-1}$ by McMullin et al. (1994). SMM 2 does not show any compact emission, consistent with the interpretation that this core does not contain a protostar.

5.1.1. SMM 1

A compact, $\sim 10''$ (4000 AU) diameter core around SMM 1 is traced by the OVRO observations of C^{18}O , H^{13}CO^+ , and H^{13}CN 1–0. Assuming local thermodynamic equilibrium (LTE), a fiducial estimate of the kinetic temperature of 30 K, and a C^{18}O abundance with respect to H_2 of 2×10^{-7} , a mass of $0.25 M_\odot$ is inferred over a $20'' \times 20''$ region. Although this appears much less than the mass of $8.7 M_\odot$ inferred from the dust emission in §4.2, modeling in §5.3 indicates that for the derived envelope parameters only a low fraction of the mass is indeed recovered through C^{18}O emission in the OVRO beam.

The emission from optically thick HCO^+ , HCN , and ^{13}CO lines appears to be directly associated with the outflow. Because of the large level of resolved-out emission in these lines, only red and blue shifted material is traced by the interferometer, whereas the bulk of the emission from the envelope is not seen. This is especially apparent in ^{13}CO , where only unresolved emission is recovered, but with a total velocity width of almost 10 km s^{-1} . The emission of HCO^+ and HCN apparently traces the walls of the outflow cavity. The position angle of the outflow is constrained by radio measurements to roughly -50° (Rodríguez et al. 1989), bisecting the two arms seen in HCN , and the roughly cross-shaped HCO^+ emission. Only the peak of the emission, centered on the protostar, has a velocity extent of $\sim 20 \text{ km s}^{-1}$ in the HCO^+ and HCN spectra. The extended ‘arms’ lie within $\sim 5 \text{ km s}^{-1}$ of the systemic velocity. H_2 emission at $2.2 \mu\text{m}$ coincides with the northern HCO^+ and HCN arm, probably tracing shocked material along the wall of the outflow (cf. Rodríguez et al. 1989). N_2H^+ 1–0 emission coincides with the northern outflow wall, but the lines are much narrower than those of HCO^+ , suggesting association with the envelope only.

Emission from SiO 2–1 and SO 2₂–1₁ coincides with the southeast outflow lobe. The prominent blue line wing in the spectrum at the emission peak at the southeast tip of the lobe clearly shows the association of SiO with material in the outflow. Using the C^{18}O upper limit at the peak of the SiO and SO emission, and assuming LTE excitation at $\sim 100 \text{ K}$, yields lower limits to the abundance of a few times 10^{-8} for SiO and $\sim 10^{-7}$ for SO . Such enhanced abundances of SiO and SO are attributed to shocked material (cf. Bachiller 1996; van Dishoeck & Blake 1998). More accurate constraints on the SiO and SO abundances require that the missing zero-spacing flux of SiO , SO , and C^{18}O be taken into account. Such detailed modeling is also required to investigate the relation between the material traced in SiO and SO compared to HCO^+ and HCN .

In ^{12}CO 2–1 maps presented by White et al. (1995) the outflow shows a complicated structure with the northwestern outflow lobe being mostly blue shifted, while the southeastern lobe shows both red- and blue-shifted emission. The small scale structure associated with the outflow also is markedly asymmetric. In H_2 at $2.2\text{ }\mu\text{m}$, and in HCO^+ and N_2H^+ in the OVRO beam the northern cavity wall is most prominent, while HCN only traces the northern and western walls. SiO and SO emission trace the southeastern outflow lobe. This asymmetry might be explained by a large-scale density gradient in the ambient medium, with denser material located to the east, coincident with the location of the bulk of the Serpens cloud. In such a medium, the time scale to clear an outflow cavity to the southeast may be longer than that to the northwest. SiO and SO emission trace shock interaction of the latter outflow lobe with ambient material, while the larger column of material is optically thick to any associated HCO^+ or HCN emission. For $n_{\text{H}_2} \approx 10^6\text{ cm}^{-3}$ and $T_{\text{kin}} \approx 30\text{ K}$, a column of a few times 10^{14} cm^{-2} in HCO^+ or HCN is sufficient for the required level of obscuration. With the envelope parameters derived in §4.2, this corresponds to a density contrast of a factor of a few between both sides of the envelope. To the northwest, HCO^+ and HCN emission arises in the walls surrounding a relatively empty outflow cavity, and H_2 $2\text{ }\mu\text{m}$ emission is observable where the outflow breaks out of the cloud.

5.1.2. SMM 2

SMM 2 only shows emission from ^{13}CO , HCO^+ , H^{13}CO^+ , and HCN in clumps scattered throughout the field of view. The spectra toward the emission peaks reveal narrow lines of 1 km s^{-1} width, except for ^{13}CO . This lack of central condensation is consistent with the upper limit on the continuum emission from §4.1, and supports the interpretation that the SMM 2 core does not contain a protostar. Instead, the interferometer appears to trace irregular structure in the extended cloud, with most of the emission distributed on large, resolved-out scales.

5.1.3. SMM 3

The ^{13}CO emission toward this source traces a $10''$ (4000 AU) diameter core around the continuum position, with a mass of $0.08\text{ }M_\odot$, while only weak emission is detected in C^{18}O . Model calculations in §5.2 confirm that only a small fraction of the $3.0\text{ }M_\odot$ envelope is recovered in ^{13}CO emission in the OVRO beam. The HCO^+ and HCN images show elongated emission extending over $\sim 30''$ at a position angle of -20° . Herbst et al. (1997) have detected a string of H_2 emission knots along a line with the same orientation, which they attribute to a jet. In this interpretation, HCO^+ and HCN trace a highly collimated outflow. Marginally detected SiO coincides with the south end of the outflow. The high degree of collimation of the outflow may indicate that SMM 3 is a particularly young YSO. Together with the projected location of SMM 3 on the edge of the outflow of SMM 4 (see below, and Fig. 4), this may suggest induced star formation. Barsony et al. (1998) suggest a similar scenario for the L1448N(A/B)+L1448 NW system, and for the NGC 1333

molecular cloud core by Lefloch et al. (1998).

Although the visual extinction toward SMM 3 is still very large, it does have the lowest inferred envelope mass of the three YSOs, possibly because it is forming a lower mass star. It is therefore probably less deeply embedded than SMM 1 or 4, based on the weak detection of C^{18}O , the upper limits on H^{13}CO^+ , and the relatively shallow absorption features in the spectra. Weak H^{13}CN emission coincides with the northern outflow lobe, indicating that HCN may be strongly enhanced by the outflow.

5.1.4. SMM 4

The C^{18}O , H^{13}CO^+ , and N_2H^+ emission traces a $5''\text{--}10''$ (2000–4000 AU) core around this source with a mass of $0.15 M_\odot$. As for SMM 1 and 3, modeling in §5.3 indicates that the amount of material traced by C^{18}O in the OVRO beam is consistent with the parameters of the $5.3 M_\odot$ envelope derived in §4.2. As explained above, the integrated ^{13}CO intensity image does not show any emission because of the large optical depth of resolved-out extended emission, so that the ^{13}CO spectrum reveals a deep absorption feature close to the systemic velocity.

In HCO^+ and HCN the emission is again associated with the outflow. The ^{12}CO 2–1 single-dish observations of White et al. (1995) indicate a north-south orientation. Eiroa et al. (1997) present $2.2 \mu\text{m}$ observations showing a possible H_2 jet with a position angle of $\sim 10^\circ$ emanating from SMM 4. HCO^+ emission outlines the northern outflow cavity, while HCN also traces the southern outflow lobe. In addition, strong emission originates from a $10''$ core, elongated perpendicular to the outflow direction. The bulk of the HCO^+ and HCN emission occurs within $2\text{--}4 \text{ km s}^{-1}$ from line center, as seen in the spectra. This indicates that the HCO^+ and HCN lines trace envelope material which is heated, compressed, or chemically altered by the outflow, but not entrained within the outflow itself. In HCO^+ there is a 4 km s^{-1} west-to-east velocity gradient, possibly indicating rotation in the envelope and cavity walls. The hyperfine components in the HCN line confuse any velocity gradient in that line. The fact that HCO^+ emission is associated with the northern outflow lobe only may be connected to a higher outflow or interaction activity on that side, in contrast to SMM 1 where the asymmetry of the HCO^+ and HCN emission may be due to increased density and opacity on the southeast side. The ^{12}CO 2–1 outflow maps of White et al. (1995) also show more intense outflow emission toward the north of SMM 4. A number of marginally detected clumps of SiO are seen close to the center of SMM 4, but no SO is found.

5.2. Single-dish results

This section discusses the single-dish observations. These data lack the spatial resolution of the interferometer results, but include higher excitation lines, so that the warmer and denser gas can be probed. In addition, they allow deep searches for lines of less abundant molecules which

are important for constraining the chemistry. Figure 6 shows the spectra obtained toward the source positions. The velocity-integrated maps are presented in Fig. 7. Table 7 lists the integrated line intensities in all observed transitions, together with estimates of the opacity averaged over the line profile. These are derived from measurements of the same transition in different isotopes, assuming isotope ratios of $[^{13}\text{C}] : [^{12}\text{C}] = 1 : 65$ and $[^{18}\text{O}] : [^{17}\text{O}] : [^{16}\text{O}] = 5 : 1 : 2695$ (Wilson & Rood 1994). Opacities at line center are much larger, as evidenced by deep self-absorption features evident in many lines.

The observed line profiles of the optically thick ^{12}CO , HCO^+ , and HCN lines are characterized by $\sim 20\text{--}30 \text{ km s}^{-1}$ wide line wings and deep, narrow ($\sim 1\text{--}2 \text{ km s}^{-1}$) self-absorption features, in addition to $2\text{--}4 \text{ km s}^{-1}$ FWHM line cores. Toward SMM 3 and 4 the blue asymmetry characteristic of infall is present in the ^{12}CO and HCO^+ lines (cf. Gregersen et al. 1997). The same lines toward SMM 1 show symmetric profiles, however. In optically thin tracers like H^{13}CO^+ , C^{18}O , C^{17}O , and H^{13}CN only a simple Gaussian line of $\sim 2 \text{ km s}^{-1}$ FWHM is seen. From the C^{17}O and C^{18}O lines systemic velocities of the sources are derived to be $+8.5 \text{ km s}^{-1}$ (SMM 1), $+7.6 \text{ km s}^{-1}$ (SMM 2), $+7.9 \text{ km s}^{-1}$ (SMM 3), and $+7.9 \text{ km s}^{-1}$ (SMM 4). The ^{13}CO lines show moderate self-absorption and $\sim 10 \text{ km s}^{-1}$ wide wings. Many of the other observed transitions show simple Gaussian line profiles, although some lines (e.g., H_2CO 3₀₃–2₀₂ and 3₂₂–2₂₁) are unresolved at the velocity resolution obtained. Hurt et al. (1996b) present observations of these lines at higher spectral resolution, which reveal moderate self-absorption features. The integrated line intensities are unaffected, as long as the overall line width is still comparable to the instrumental resolution.

The ^{12}CO 4–3 and 6–5 line profiles of Fig. 6 reveal an interesting hint about the temperature and velocity structure of the outflowing gas. While the line wings in ^{12}CO 4–3 decrease smoothly to more red and blue-shifted velocities, the ^{12}CO 6–5 wings show secondary maxima at $\sim 7\text{--}9 \text{ km s}^{-1}$ from the systemic velocity. This indicates that the excitation temperature of the gas increases with velocity in the outflow, to $\gtrsim 200 \text{ K}$ at the velocity of the secondary maxima in ^{12}CO 6–5. In addition, a larger fraction of the 6–5 line cores is self-absorbed as compared to the 4–3 lines. The ^{12}CO 6–5 line profiles toward the low-mass YSO TMC 1A in Taurus show a similar secondary maximum in the blue line wing (Hogerheijde et al. 1998).

The maps of integrated intensity show well-defined cores around SMM 1, 3, and 4. Again, SMM 2 appears associated with a condensation in the overall cloud rather than a YSO. Still, SMM 2 does show ^{12}CO 6–5 emission with broad line wings, which requires kinetic temperatures of 80 K or more to be excited, as well as the secondary maxima noted above. White et al. (1995) conclude from ^{12}CO 2–1 mapping that outflow emission permeates the whole Serpens cloud core region. Probably, the ^{12}CO 6–5 lines are tracing this same material at the position of SMM 2 with the same distribution of excitation temperature with velocity. The ^{12}CO 4–3, and HCO^+ 3–2 and 4–3 maps toward SMM 1, 3, and 4 are resolved with diameters of $20''\text{--}30''$ (8000–12000 AU), while H^{13}CO^+ 3–2 (SMM 1) and HCN 4–3 (SMM 1 and 4) appear unresolved at the respective beam sizes of $19''$ (7600 AU) and $14''$ (5600 AU). The maximum of the emission in ^{12}CO 4–3 toward SMM 4 is offset by $\sim 15''$ to the north. The five-point map observed in ^{12}CO 6–5 shows a similar

offset. These lines probably trace $T_{\text{kin}} \approx 100$ K gas associated with the outflow. Absorption of a significant fraction of the line profiles by cold and dense envelope material within $\sim 15''$ from the YSO could explain the apparent offsets of the peak in the integrated intensity maps.

5.3. A model for the molecular line emission

Section 4.2 described a model for the envelope based on the dust continuum emission, with $\rho \propto r^{-2}$ and $T_{\text{d}} \propto r^{-0.4}$. Although the inner few hundred AU of the envelope is relatively warm, 80% of the material is below the ~ 30 K required to excite many of the observed molecular lines. Therefore, an important question is if the envelope model can reproduce the observed line emission. Related issues are the limits set by the data on the molecular abundances, and on their possible depletion by freezing out onto dust grains.

We use a Monte-Carlo code recently developed by Hogerheijde & van der Tak (1998) to solve the non-LTE excitation and line transfer in a spherically symmetric envelope with the density and temperature distribution of §4.2. An inner radius of 100 AU is adopted, which does not influence the results. The core is assumed to be static with a turbulent width that is constant with radius. FWHM values of 1.4 km s⁻¹ for SMM 1, 2.1 km s⁻¹ for SMM 3, and 2.0 km s⁻¹ for SMM 4 reproduce the observed FWHM line width of the C¹⁷O, C¹⁸O, and H¹³CO⁺ lines. The effect of neglecting any systematic velocity field, like infall, is to increase the optical depth for material close to the center, thereby decreasing the integrated intensity of optically thick lines of ¹²CO, HCO⁺, and HCN (cf. Hogerheijde 1998; Hogerheijde & van der Tak 1998). Because of the imperfect thermal coupling between gas and dust, and the cooling of the gas through line radiation, the gas temperature may be lower than that of the dust. Self-consistent models by Ceccarelli et al. (1996) and Doty & Neufeld (1997) suggest $T_{\text{kin}} = (0.6\text{--}0.8) \times T_{\text{dust}}$.

The molecular abundances are a free parameter of the model, in addition to the exact relation between T_{kin} and T_{dust} . Standard isotopic ratios are assumed (Wilson & Rood 1994), as well as an ortho-to-para ratio of 3:1 for H₂CO and C₃H₂. The abundance of ¹²CO is fixed at the ‘standard’ value of 10⁻⁴ with respect to H₂, except for the possibility of depletion onto dust grains. In our model, CO is allowed to freeze out on dust grains when the temperature drops below the sublimation temperature of 20 K (Sandford & Allamandola 1990, 1993). Absorption studies toward nearby infrared sources provide evidence for solid CO in the Serpens cloud (Chiar et al. 1994), with $\sim 40\%$ of the total CO column frozen out onto grains. The optically thin C¹⁸O 2–1 and C¹⁷O 3–2 lines set limits both on the depletion and the relation between T_{kin} and T_{dust} . Assuming $T_{\text{kin}} = T_{\text{dust}}$ and no CO depletion, the model overestimates the C¹⁸O 2–1 and C¹⁷O 3–2 intensities by factors of 1.5–2.0 for the different sources. A better fit is found by adopting $T_{\text{kin}} < T_{\text{dust}}$ or by depleting CO in the coldest region of the cloud. A lower limit of $T_{\text{kin}} = (0.7\text{--}0.8) \times T_{\text{dust}}$ is found if CO is undepleted. Alternatively, the observed intensities are reproduced if CO is depleted by a factor of 3–10 for SMM 1, 2–4 for SMM 3, and 2–4 for SMM 4 in regions with $T_{\text{kin}} < 20$ K, using $T_{\text{kin}} = T_{\text{dust}}$. This provides a slightly better fit to the data,

since C^{18}O 2–1, which traces 16 K gas, is more strongly affected than C^{17}O 3–2, which traces 30 K gas. These depletion factors are maximum values; less depletion is found for $T_{\text{kin}} < T_{\text{dust}}$. These results depend on the adopted dust emissivity, but the depletion would be much larger only if the emissivity were overestimated by a large factor. The data therefore show that molecules are not strongly depleted in these sources (cf. §6.2).

Table 8 lists the molecular abundances derived from the observations using the envelope model. For simplicity, the calculations assume $T_{\text{kin}} = T_{\text{dust}}$ and the derived depletion factors in regions with $T_{\text{kin}} < 20$ K. None of these assumptions influences the results by more than a factor of 2, especially since most observed transitions only trace material with $T_{\text{kin}} > 30$ K. The inferred abundances ('envelope' column of Table 8) are compared to results for another class 0 YSO, IRAS 16293–2422 (van Dishoeck et al. 1995). The values of most species agree within a factor of 2 to 3. SiO and SO have smaller inferred values toward the Serpens sources, because our single-dish beams did not contain the emission peak apparent in the interferometer images (cf. 5.1). Other differences are found toward SMM 1, where the abundances of CN, HC_3N , and C_3H_2 are larger by an order of magnitude compared to IRAS 16293–2422. The inferred abundance of C I is highly uncertain. With its critical density of only 10^3 cm^{-3} , the [C I] ${}^3\text{P}_1 - {}^3\text{P}_0$ line is likely to trace the low-density surface of the entire Serpens cloud, where the interstellar radiation field has returned much of the carbon in the atomic phase. White et al. (1995) reach that same conclusion from the lack of [C I] emission maxima at the positions of the submillimeter cores.

Most lines are well reproduced for these envelope parameters. Notable exceptions are the optically thick ${}^{12}\text{CO}$ lines, for which the treatment of the velocity field is too simple and where the outflow also contributes significantly, and high excitation lines like ${}^{13}\text{CO}$ 6–5 and H_2CO 3₂₂–2₂₁. This indicates the presence of more warm, $T_{\text{kin}} \sim 100$ K, material than can be accounted for by the model. The line ratio of H_2CO 3₀₃–2₀₂ over 3₂₂–2₂₁ is a very sensitive diagnostic of kinetic temperature (Mangum & Wootten 1993; Jansen, van Dishoeck, & Black 1994; Hurt et al. 1996b). Our data imply a gas density in excess of 10^6 cm^{-3} , and a kinetic temperature of 50–200 K, consistent with the findings of Hurt et al. (1996b). Adopting the parameters derived by these authors, the excess ${}^{13}\text{CO}$ 6–5 emission is reproduced by column densities of $7 \times 10^{21} \text{ cm}^{-2}$ toward SMM 1, $1 \times 10^{21} \text{ cm}^{-2}$ toward SMM 3, and $5 \times 10^{20} \text{ cm}^{-2}$ toward SMM 4. This material, less than 1% of the total envelope mass, may be associated with the inner few hundred AU of the envelopes where the temperature exceeds the adopted power-law distribution, or with the outflows, as suggested by the ${}^{13}\text{CO}$ and ${}^{12}\text{CO}$ line wings. It contributes no more than 10% to the total continuum flux, and, if confined to the inner 1000 AU, could explain the point source fluxes required to fit the interferometer continuum observations of §4.2. Could this material dominate the emission in the other observed molecular lines? Table 8 ('warm gas' column) lists the molecular abundances derived under the assumption that this component is responsible for all observed emission except CO. All values are larger by an order of magnitude compared to those found from the 'cold envelope', indicating that the warm gas may contribute significantly to the observed intensities, but only if the abundances are much enhanced.

On the 300–4000 AU scales sampled by the interferometer, the envelope model predicts line intensities within a factor of 5 of the observed values for most lines. To derive these intensities, the model data have been sampled at the same (u, v) positions as the observations. In §§5.1.1–5.1.4 masses were derived from the ^{13}CO and C^{18}O lines observed with OVRO which were 30 times smaller than the values derived in §4.2 from the dust emission. The results of Table 8 show that such low fractions of recovered emission can be mostly explained by the envelope parameters. This good agreement indicates that there are no strong abundance changes on small scales. However, a more realistic treatment of the velocity field and possible variations from spherical symmetry on small scales is required before stronger abundance constraints can be derived.

6. Discussion

6.1. Envelopes and disks around class 0 and I YSOs

This section compares the density structure of the Serpens class 0 YSOs studied in this paper to results for other class 0 objects and more evolved class I sources. The inferred density structure for the envelopes around the Serpens YSOs as a radial power law with a slope of -2.0 ± 0.5 agrees well with previous results for class 0 YSOs and theoretical expectations. Zhou et al. (1993) and Choi et al. (1995) find that molecular line profiles observed toward the class 0 YSOs B335 and IRAS 16293–2422 can be accurately reproduced using the inside-out collapse model of Shu (1997). This model predicts density power-law indices between -1 and -2 . Recent millimeter-continuum mapping observations of dense cores with and without embedded stars have shown that the former have density distribution with $\rho \propto r^{-p}$ with $p \approx 2$, while the latter have a significantly flatter distribution in the inner few thousand AU (Ward-Thompson et al. 1994; André, Ward-Thompson, & Motte 1996; and Motte, André, & Neri 1998). Our interferometric millimeter-continuum observations directly trace these size scales, and confirm that the envelopes around class 0 YSOs are strongly centrally concentrated.

In two recent papers (Hogerheijde et al. 1997, 1998), we investigated a sample of nine class I YSOs in Taurus through a data set which is very similar to that presented here. The millimeter continuum emission toward at least two-thirds of these class I sources is dominated by an unresolved component, presumably a disk, carrying 30%–75% of the total 1 mm flux. The point-source flux required in §4.2 to fit the interferometer continuum observations of the SMM 1, 3, and 4 amounts to only 20%–30% of the total 1.1 mm flux. This indicates that any circumstellar disk makes a much smaller relative contribution to the total flux of class 0 sources than for class I objects, especially since a sizeable fraction of this point-source emission may also be attributable to the warm, inner 100 AU of the envelope. No limits on disk masses can therefore be obtained for the Serpens class 0 sources from the present data.

Significant, resolved emission around the Taurus class I sources was only detected toward L1551 IRS 5 and L1527 IRS. The visibility fluxes of the latter source, which is sometimes referred

to as a class 0 source, closely resemble those of the Serpens class 0 YSOs, but its total envelope mass is only $0.03 M_{\odot}$, and the signal-to-noise is insufficient to fit an envelope model as in §4.2. The envelopes around all Taurus class I sources, including L1527 IRS, contain less than 50% of the estimated stellar mass, consistent with their higher age. Because of their lower masses, these envelopes of class I sources are much better traced by molecular lines than by continuum emission. HCO^+ 1–0, 3–2, and 4–3 single-dish observations of the Taurus class I sources showed that their envelopes are well described by a power-law density structure, similar to that derived here for the Serpens class 0 objects. From the integrated intensities observed by Hogerheijde et al. (1997), the power-law slope is constrained to lie between -1 and -3 . These values are consistent with predicted values of -1 to -2 for a collapsing cloud (Shu 1977), and with the values for the class 0 sources found here. By including the complete observed line profile in the model fit, much more accurate constraints on age and envelope density structure can be obtained, which will allow tests of other collapse models (cf. Zhou 1992, 1995; Zhou et al. 1993; Walker, Narayanan, & Boss 1994; Choi et al. 1995; Hogerheijde 1998; Hogerheijde & van der Tak 1998).

The Serpens YSOs studied in this paper have formed within a projected distance of 25,000 AU of each other. The detection of widespread emission from moderate J lines of CO with broad profiles (White et al. 1995) indicates that material throughout the Serpens cloud is influenced by the outflows. It is therefore remarkable that our data, which probe the 16,000 AU diameter envelopes on 1000 AU scales, are consistent with the density structure predicted for the formation of an isolated star (Shu 1977; §4.2). This suggests that the influence of the outflows on the cloud structure is largely confined to lower density material, leaving the dense cores mostly unaffected. Alternatively, their envelopes may reflect the original, relatively isolated state if all three YSOs have formed within an interval shorter than the dynamic time scale of the outflows of ~ 8000 yr as estimated from the ^{12}CO 2–1 data of White et al. (1995). However, the projected location of SMM 3 at the edge of the outflow driven by SMM 4, and the small age suggested by the highly collimated nature of SMM 3’s outflow as traced by HCN 1–0, may indicate induced star formation. Single-dish mapping of the entire cloud on $10''$ – $15''$ scales, which are well matched to the interferometer observations, are required to further investigate the influence of star formation on the cloud structure. Such observations may also shed further light on the nature of the apparently starless core SMM 2 and the ~ 30 low-mass cores identified recently by Testi & Sargent (1998) from an extensive interferometric survey of the Serpens cloud core.

6.2. Molecular abundances in class 0 envelopes

The model results of §5.3 indicate that CO is depleted by factors of 2–10 in the cold regions of the envelopes where $T_{\text{kin}} < 20$ K, its sublimation temperature, but not in the warmer inner regions of the envelope. Such a level of depletion is small compared to the value of 10–20 inferred for the bulk of the envelope of two other class 0 YSOs, NGC 1333 IRAS 4A and B (Blake et al. 1995). Submillimeter observations of the latter sources indicate envelope masses of 9 and $4 M_{\odot}$

in a 20" beam, adopting a distance of 350 pc, comparable to or larger than those of the Serpens sources. Based on a detailed excitation analysis, Blake et al. conclude that the abundances of all molecules including CO are depleted by a factor of 10–20 when the dust emission is used as a reference to determine the total column density. Blake et al. used a value for the dust emissivity which was smaller by a factor of 2 than the value adopted by us. If the same value had been assumed, their derived depletion would be even larger, increasing the difference with the depletion we find toward the Serpens sources. This highlights the difficulty in deriving and interpreting molecular depletion (cf. Mundy & McMullin 1997). The large difference in molecular depletion between class 0 YSOs which are otherwise very similar suggests that the quiescent evolutionary phase characterized by heavily depleted abundances may be relatively short-lived. In addition, the local star-formation density may be important. The largest levels of CO depletion are inferred for the relatively isolated NGC 1333 IRAS 4 object; lower values are found toward SMM 1, which is located in the northwest of the Serpens region, while the lowest values are inferred for SMM 3 and 4, at the very center of the densely star forming cloud. Possibly the high density of star formation activity inhibits CO depletion, suggesting that the chemistry may be more sensitive to the environment than the physical structure of the envelopes (cf. previous section).

The line profile shapes toward NGC 1333 IRAS 4A and B resemble those of the Serpens sources. Blake et al. conclude that the HCN 4–3 profile, which is significantly broader than, e.g., HCO^+ 4–3, indicates that HCN may be enhanced in the outflow. Our HCN 4–3 spectra show this same trend. In the interferometer beam, H^{13}CN 1–0 peaks toward the northern outflow lobe of SMM 3, supporting the interpretation of larger abundances in the outflow. Enhanced abundances of volatile species like H_2CO and CH_3OH toward NGC 1333 IRAS 4A and B are attributed by Blake et al. to grain-grain collisions in the velocity-shear zones surrounding the outflow. These collisions heat the dust grains transiently and evaporate the ice mantles. Thus, the dynamic interaction of the outflow with the surrounding envelope could explain the bright emission of some species outlining the walls of the outflow cavities of YSOs.

7. Summary

Continuum and molecular-line emission from four protostellar candidates in the Serpens Molecular Cloud (SMM 1 = FIRS 1, SMM 2, SMM 3, and SMM 4) has been used to provide the first comprehensive picture of the physical and chemical structure on 1000–10,000 AU scales in a clustered region. We confirm the nature of SMM 1, 3, and 4 as deeply embedded, class 0 YSOs with more than 50% of their total mass still in a circumstellar envelope. The density in these envelopes is well described by a power-law with slope -2.0 ± 0.5 . This agrees with theoretical predictions for an isolated cloud core, even though the SMM 1, 3, and 4 are in close proximity of each other, and outflowing gas permeates the whole Serpens core. The characteristics of, at least, the early phases of star formation therefore do not seem to be very different between isolated and more clustered environments. Large degrees of molecular depletion by freezing-out of molecules

onto grains have been inferred for some class 0 YSOs, but the low levels of depletion found toward the Serpens sources suggests this phase may be short-lived and/or influenced by the surrounding star-forming activity. SMM 2 is most likely a warm cloud condensation without a central object since it shows no compact continuum or molecular line emission. The main conclusions of this paper can be summarized as follows:

1. The interferometric observations of SMM 1, 3, and 4 in 3.4–1.4 mm dust continuum emission are excellent tools to derive the structure of the envelopes surrounding these class 0 sources. They are characterized by intense, resolved ($> 2'' = 800$ AU) emission which can be described by a density distribution that follows a radial power law with index -2.0 ± 0.5 . Such a density distribution agrees well with model predictions for the earliest phases of protostellar collapse (e.g., Shu 1977). The temperature distribution is based on self-consistent model results, and fits to the millimeter and far-infrared SED. At a representative radius of 1000 AU, dust temperatures of 27 K (SMM 1), 24 K (SMM 3), and 20 K (SMM 4) are found. The mass contained within the envelopes is constrained to $8.7 M_\odot$ for SMM 1, $3.0 M_\odot$ for SMM 3, and $5.3 M_\odot$ for SMM 4. To fit the flux on long baselines, a point source with 20%–30% of the total flux is required, corresponding to emission originating from radii < 100 AU. Observations at higher spatial resolution are required to investigate how much of this flux is due to a circumstellar disk and how much to the dense inner 100 AU of the power-law envelope. Such observations for other class 0 YSOs suggests the envelope dominates the emission even on small scales.
2. The aperture-synthesis molecular line observations reveal $5''$ – $10''$ (2000–4000 AU) diameter cores around SMM 1, 3, and 4 in C^{18}O , ^{13}CO , H^{13}CO^+ , and H^{13}CN . The HCO^+ and HCN emission traces the walls of the outflow cavities, while SiO and SO emission originates from material shocked by the outflows. Molecular species and transitions are thus identified which selectively probe different physical regions of the envelope, offering diagnostic tools for future studies of the protostellar environment.
3. Higher excitation single-dish lines show broad outflow wings and deep, narrow self-absorption features, in addition to Gaussian line cores of 2 – 3 km s^{-1} FWHM. Monte-Carlo calculations of the molecular excitation and line transfer show that the envelope model derived from the dust emission can successfully reproduce the observed single-dish and interferometric line intensities, except for the $\lesssim 1\%$ of warm material traced in the ^{12}CO , ^{13}CO 6–5, and some of the H_2CO lines. The CO abundance appears to be decreased by a factor of 2–6 in the regions of the envelope where the gas temperature is 20 K or less ($r > 2000$ AU), owing perhaps to freezing-out onto grains. The derived molecular abundances in the warmer gas ($T_{\text{kin}} > 20$ K) are comparable to those found toward other class 0 YSOs, but some species may be enhanced toward SMM 1. The model predicts interferometric line fluxes which are within a factor of a few of the observed values, indicating that there are no large abundance variations on 300–4000 AU scales. However, a more realistic treatment of the velocity field and possible deviations from spherical symmetry have to be included before firmer limits can be placed on the abundances.

The authors are grateful to the staffs of the JCMT, CSO, and OVRO telescopes for their assistance. Remo Tilanus and Fred Baas are thanked for carrying out part of the JCMT observations. Lee Mundy and Huib Jan van Langevelde are acknowledged for useful discussions. Floris van der Tak kindly assisted in deriving the self-consistent temperature structure of the envelopes. M. R. H. is indebted to the Caltech Divisions of Geological and Planetary Sciences and Mathematics, Physics and Astronomy, and the Owens Valley Radio Observatory for their hospitality, and to the Netherlands Organization for Scientific Research (NWO) and the Leids Kerkhoven-Bosscha Fonds for travel support. Research in Astrochemistry in Leiden is supported by NWO/NFRA through grant no. 781–76–015. G. A. B. gratefully acknowledges support provided by NASA grants NAG5–4383 and NAG5–3733. A critical reading by Xander Tielens and many valuable comments by the referee helped to improve the presentation.

REFERENCES

Adams, F. C., Lada, C. J., & Shu, F. H. 1987, *ApJ*, 312, 788

Agladze, N. I., Sievers, A. J., Jones, S. A., Burlitch, J. M., & Beckwith, S. V. W. 1994, *Nature*, 372, 243

André, Ph., Martín-Pintado, J., Despois, D., & Montmerle, T. 1990, *A&A*, 236, 180

André, Ph., Ward-Thompson, D., & Barsony, M. 1993, *ApJ*, 406, 122

André, Ph., Ward-Thompson, D., & Motte, F. 1996, *A&A*, 314, 625

Bachiller, R., 1996, *ARA&A*, 34, 111

Bachiller, R., & Pérez Gutiérrez, M. 1997, *ApJ*, 487, L93

Blake, G. A., van Dishoeck, E. F., Jansen, D. J., Groesbeck, T. D., & Mundy, L. G. 1994, *ApJ*, 428, 680

Blake, G. A., Sandell, G., van Dishoeck, E. F., Groesbeck, T. D., Mundy, L. G., & Aspin, C. 1995, *ApJ*, 441, 689

Boss, A. P. 1993, *ApJ*, 410, 157

Calvet, N., Hartmann, L., & Strom, S. E. 1997, *ApJ*, 481, 912

Casali, M. M., Eiroa, C., & Duncan, W. D. 1993, *A&A*, 275, 195

Ceccarelli, C., Hollenbach, D. J., & Tielens, A. G. G.M. 1996, *ApJ*, 471, 400

Chiar, J. E. 1996, Ph. D. Thesis (Rensselaer Polytechnic Institute, Troy)

Chiar, J. E., Adamson, A. J., Kerr, T. H., & Whittet, D. C. B. 1994, *ApJ*, 426, 240

Choi, M. H., Evans II, N. J., Gregersen, E. M., & Wang, Y. S. 1995, *ApJ*, 448, 742

de Lara, E., Chavarria-K, C., & López-Molina, G. 1991, *A&A*, 243, 139

Dinger, A. S. C., & Dickinson, D. F. 1980, *AJ*, 85, 1247

Doty, S., & Neufeld, D. 1997, *ApJ*, 489, 122

Eiroa, C., & Casali, M. M. 1989, *A&A*, 223, L17

Eiroa, C., & Casali, M. M. 1992, *A&A*, 262, 468

Eiroa, C., Palacios, J., Eislöffel, J., Casali, M. M., & Curiel, S. 1997, in Low-Mass Star Formation: From Infall to Outflow, Poster Proc. IAU Symp. 182, eds. F. Malbet, A. Castets, (Grenoble: Observatoire), 103

Fiedler, R. A., & Mouschovias, T. C. 1992, *ApJ*, 391, 199

Giovannetti, P., Caux, E., Nadeau, D., & Monin, J.-L. 1998 *A&A*, 330, 990

Gregersen, E. M., Evans II, N. J., Zhou, S., & Choi, M. 1997, *ApJ*, 484, 256

Gueth, F., Guilloteau, S., Dutrey, A., & Bachiller, R. 1997, *A&A*, 323, 943

Guilloteau, S., Bachiller, R., Fuente, A., & Lucas, R. 1992, *A&A*, 256, L49

Harvey, P. M., Wilking, B. A., & Joy, M. 1984, *ApJ*, 278, 156

Herbst, T., Beckwith, S. V. W., & Robberto, M. 1997, *ApJ*, 486, L59

Hirano, N., Kameya, O., Mikami, H., Saito, S., Umemoto, T., & Yamamoto, S. 1997, *ApJ*, 478, 631

Hogerheijde, M. R. 1998, Ph. D. Thesis (Leiden University)

Hogerheijde, M. R., van Dishoeck, E. F., Blake, G. A., & van Langevelde, H. J. 1997, *ApJ*, 489, 293

Hogerheijde, M. R., van Dishoeck, E. F., Blake, G. A., & van Langevelde, H. J. 1998, *ApJ*, 502, 315

Hogerheijde, M. R., & van der Tak, F. F. S. 1998, in preparation.

Hurt, R. L., & Barsony, M. 1996a, *ApJ*, 460, L45

Hurt, R. L., Barsony, M., & Wootten, A. 1996b, *ApJ*, 456, 686

Jansen, D. J., van Dishoeck, E. F., & Black, J. H. 1994, *A&A*, 282, 605

Langer, W. D., Velusamy, T., & Xie, T. 1996, *ApJ*, 468, L41

Lefloch, B., Castets, A., Cernicharo, J., Langer, W. D., & Zylka, R. 1998, *A&A*, 334, 269

Lizano, S., & Shu, F. H. 1989, *ApJ*, 342, 834

Mangum, J. G., & Wootten, A. 1993, *ApJS*, 89, 123

Mardones, D., Myers, P. C., Tafalla, M., Wilner, D. J., Bachiller, R., & Garay, G. 1997, *ApJ*, 489, 719

McMullin, J. P., Mundy, L. G., Wilking, B. A., Hezel, T., & Blake, G. A. 1994, *ApJ*, 424, 222

Motte, F., André, Ph., & Neri, R. 1998, *A&A*, 336, 150

Mundy, L. G., & McMullin, J. P. 1997, in *Molecules in Astrophysics: Probes and Processes*, Proc. IAU Symp. 178, ed. E. F. van Dishoeck (Dordrecht: Kluwer Academic Publishers), 183

Nordh, H. L., Fridlund, C. V. M., van Duinen, R. J., Sargent, A. I., Aalders, J. W. G., & Beintema, D. 1982, *A&A*, 115, 308

Ossenkopf, V., & Henning, Th. 1994, *A&A*, 291, 943

Pollack, J. B., Hollenbach, D., Beckwith, S. V. W., Simonelli, D. P., Roush, T., & Fong, W. 1994, *ApJ*, 421, 615

Pudritz, R. E., Wilson, C. D., Carlstrom, J. E., Lay, O. P., Hills, R. E., & Ward-Thompson, D. 1996, *ApJ*, 470, L123

Rodríguez, L. F., Moran, J. M., Gottlieb, E. W., & Ho, P. T. P. 1980, *ApJ*, 235, 845

Rodríguez, L. F., Curiel, S., Moran, J. M., Mirabel, I. F., Roth, M., & Garay, G. 1989, *ApJ*, 346, L85

Rowan-Robinson, M. 1980, *ApJS*, 44, 403

Sandford, S. A., & Allamandola, L. J. 1990, *Icarus*, 87, 188

Sandford, S. A., & Allamandola, L. J. 1993, *ApJ*, 417, 815

Scoville, N. Z., Carlstrom, J. E., Chandler, C. J., Phillips, J. A., Scott, S. L., Tilanus, R. P. J., & Wang, Z. 1993, *PASP*, 105, 1482

Shu, F. H. 1977, *ApJ*, 214, 488

Terebey, S., Shu, F. H., & Cassen, P. 1984, *ApJ*, 286, 529

Testi, L., & Sargent, A. I. 1998, *ApJ*, in press

van der Tak, F. F. S., van Dishoeck, E. F., Evans II, N. J., & Blake, G. A. 1998, *ApJ*, submitted.

van Dishoeck, E. F., Blake, G. A., Jansen, D. J., & Groesbeck, T. D. 1995, *ApJ*, 447, 760

van Dishoeck, E. F., & Blake, G. A. 1998, *ARA&A*, 36, in press.

Walker, C. K., Carlstrom, J. E., & Bieging, J. H. 1993, *ApJ*, 402, 655

Walker, C. K., Narayanan, G., & Boss, A. P. 1994, *ApJ*, 431, 767

Ward-Thompson, D., Scott, P. F., Hills, R. E., & André, Ph. 1994, *MNRAS*, 268, 276

Wilson, T. L., & Rood, R. 1994, *ARA&A*, 32, 191

White, G. J., Casali, M. M., & Eiroa, C. 1995, *A&A*, 298, 594

Zhang, Q., Ho, P. T. P., Wright, M. C. H., & Wilner, D. J. 1995, *ApJ*, 451, L71

Zhou, S. 1992, *ApJ*, 394, 204

Zhou, S. 1995, *ApJ*, 442, 685

Zhou, S., Evans II, N. J., Kömpe, C., & Walmsley, C. M. 1993, *ApJ*, 404, 232

Fig. 1.— Cleaned, uniformly weighted images of continuum emission at $\lambda = 3.4, 3.2, 2.7$, and 1.4 mm of SMM 1, 2, 3, and 4 observed with OVRO. Contour levels are drawn at 3σ intervals (at $3.4, 3.2, 2.7, 1.4$ mm: $6, 9, 18, 48$ mJy beam $^{-1}$ for SMM 1; $4, \dots, 6, 90$ mJy beam $^{-1}$ for SMM 2; $6, \dots, 12, 150$ mJy beam $^{-1}$ for SMM 3; and $6, 9, 9, 45$ mJy beam $^{-1}$ for SMM 4). Synthesized beam sizes are indicated in each panel. Note the much smaller depicted region at 1.4 mm.

Fig. 2.— Vector-averaged visibility amplitudes of observed continuum emission at $3.4, 3.2, 2.7$ and 1.4 mm in mJy as functions of projected baseline length in $k\lambda$. The data are plotted as filled symbols, together with 1σ error bars. The dashed histogram shows the zero-signal expectation value. The solid lines are best-fit models as described in §4.2, for a density power-law slope of -2.0 and point source fluxes of §4.2. These model curves are not smooth because of incomplete sampling of the (u, v) plane in the original data set.

Fig. 3.— Comparison of model visibility amplitudes to observations of SMM 1. The observed vector-averaged amplitudes are indicated by the filled symbols and their 1σ error bars. Dotted lines are models without a central point source, and density power-law slopes of -1.0 (*lower curve in each panel*), -2.0 (*middle curve*), and -3.0 (*upper curve*). Solid lines are models with a point source flux of 0.13 Jy at 2.7 mm and a spectral slope of 2.0 .

Fig. 4.— (a) Cleaned, naturally weighted images of molecular line emission observed with OVRO toward SMM 1. Contours are drawn at 3σ intervals of 10 (^{13}CO), 4 (C^{18}O , SiO , HCN , H^{13}CN), 1 (HCO^+ , SO), and 8 (H^{13}CO^+ , N_2H^+) K km s $^{-1}$. The synthesized beam size is indicated in each panel. The dashed circle shows the primary beam size. The arrows in the HCN panel indicate the position angle of the 6 cm radio jet of Rodríguez et al. 1989. (b) Same, for SMM 2, 3, and 4. Contour levels are 1.5 (C^{18}O , H^{13}CO^+), 2.0 (^{13}CO , HCO^+ , HCN), 2.5 (SiO , H^{13}CN), and 3.0 (N_2H^+) K km s $^{-1}$. The images have been cleaned separately, and mosaicked afterwards. The arrows in the HCN panel indicate the position angles of the H_2 jets (from Herbst et al. 1997 and Eiroa et al. 1997)

Fig. 5.— Spectra obtained within a synthesized beam from the emission maximum of molecular lines observed with OVRO. Vertical scale is brightness temperature T_b , horizontal scale is velocity V_{LSR} . The vertical dashed line indicates the systemic velocity V_0 of the sources.

Fig. 6.— Spectra obtained in the single-dish beams. Vertical scale is main-beam temperature T_{mb} , horizontal scale is velocity V_{LSR} . The vertical dotted line indicates the systemic velocity of the source. (a) SMM 1, (b) SMM 2, (c) SMM 3, (d) SMM 4.

Fig. 7.— (a) Maps of integrated intensity observed with the JCMT toward SMM 1. Sampling is indicated by the small dots, except for HCO^+ 3–2, which is fully sampled. The dashed lines shows the extent of the mapped region. The beam sizes are indicated in each panel. Contours are drawn at approximately 3σ intervals of 20 (^{12}CO), 4 (HCO^+ 4–3), 2.4 (HCO^+ 3–2, HCN 4–3), 0.9 (H^{13}CO^+), and 0.5 (H_2CO , SO) K km s $^{-1}$. The thick contour indicates the 50% of maximum intensity level. (b) Same, for SMM 2, 3, and 4 together. The sampling, identical to that for SMM 1,

is not indicated for clarity. Contour levels are 15 K km s^{−1} for ¹²CO and 3 K km s^{−1} for HCO⁺ 3–2, 4–3 and HCN.

Fig. 1

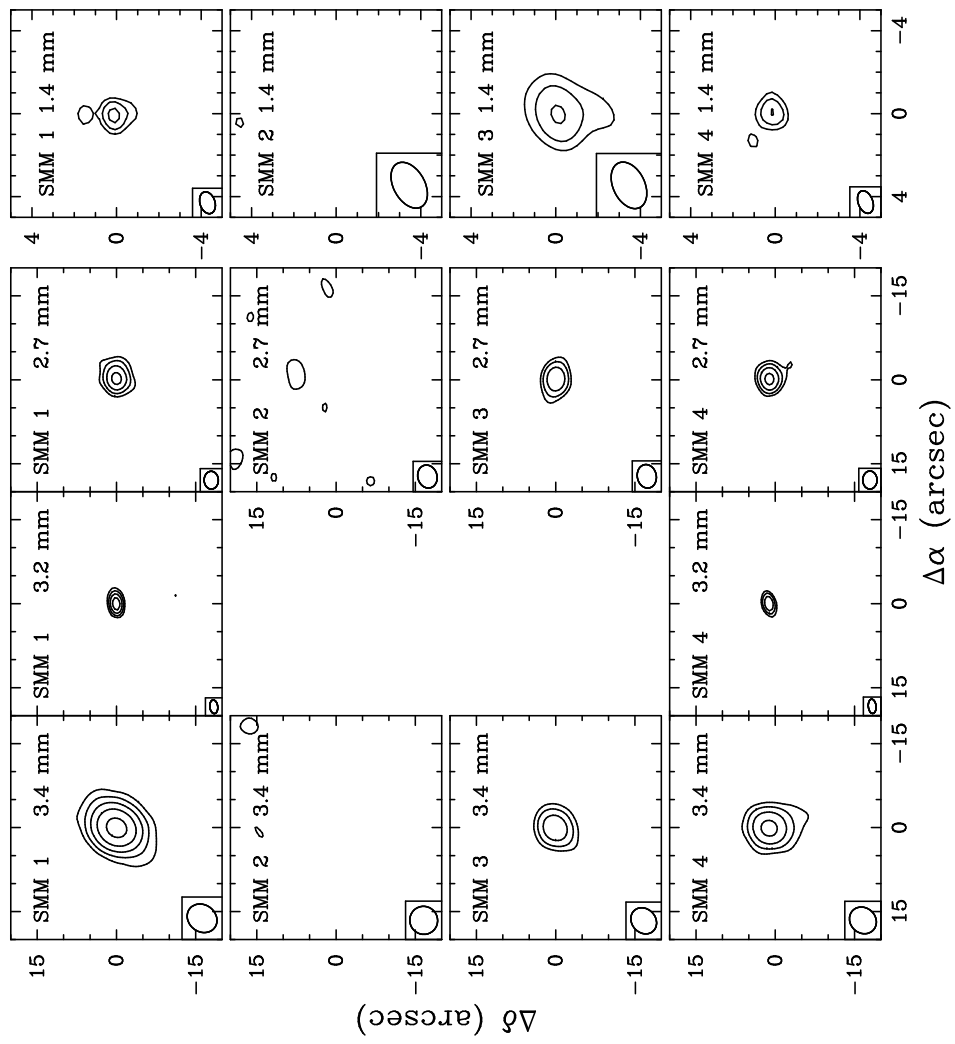


Fig. 2

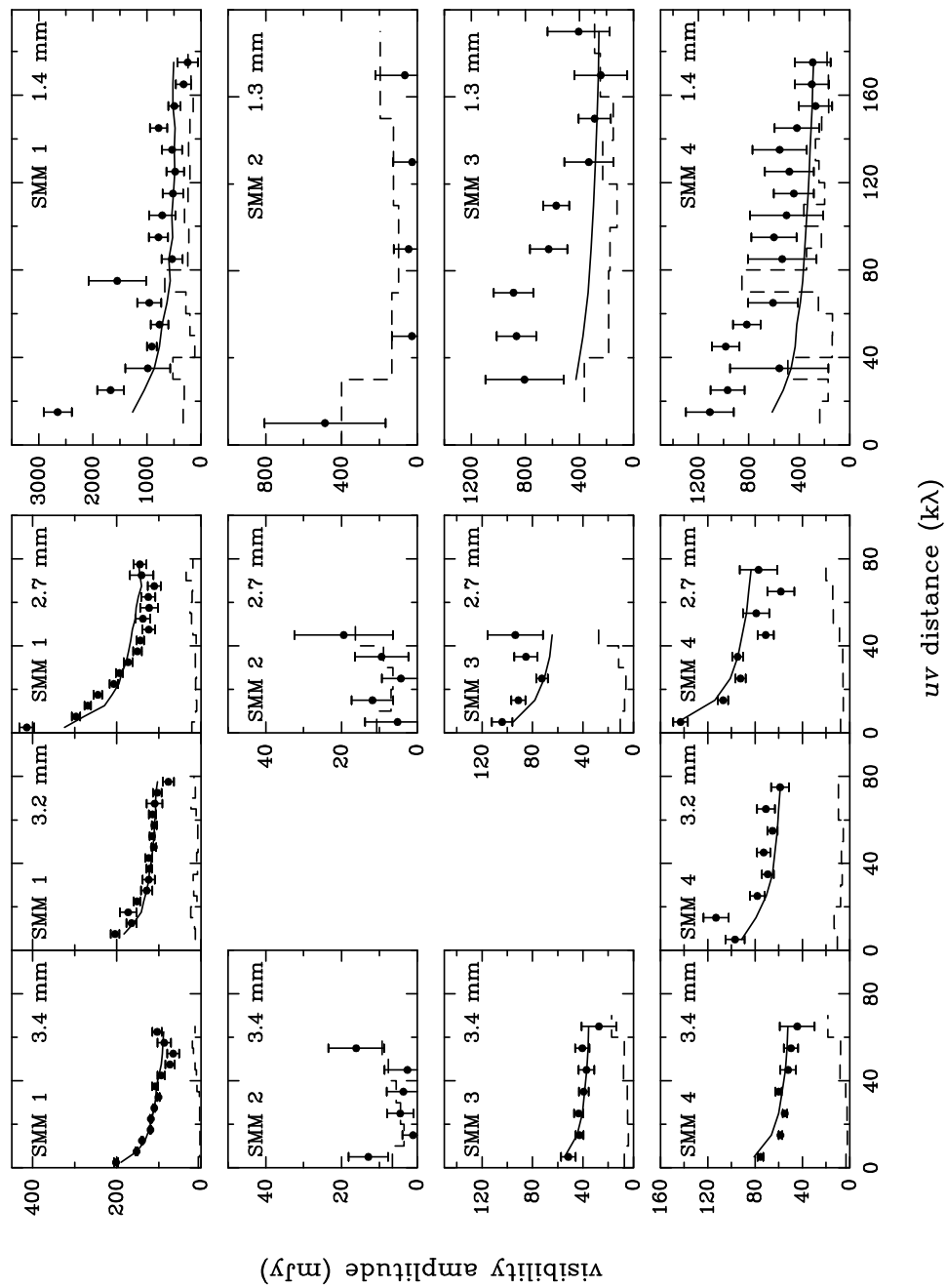


Fig. 3

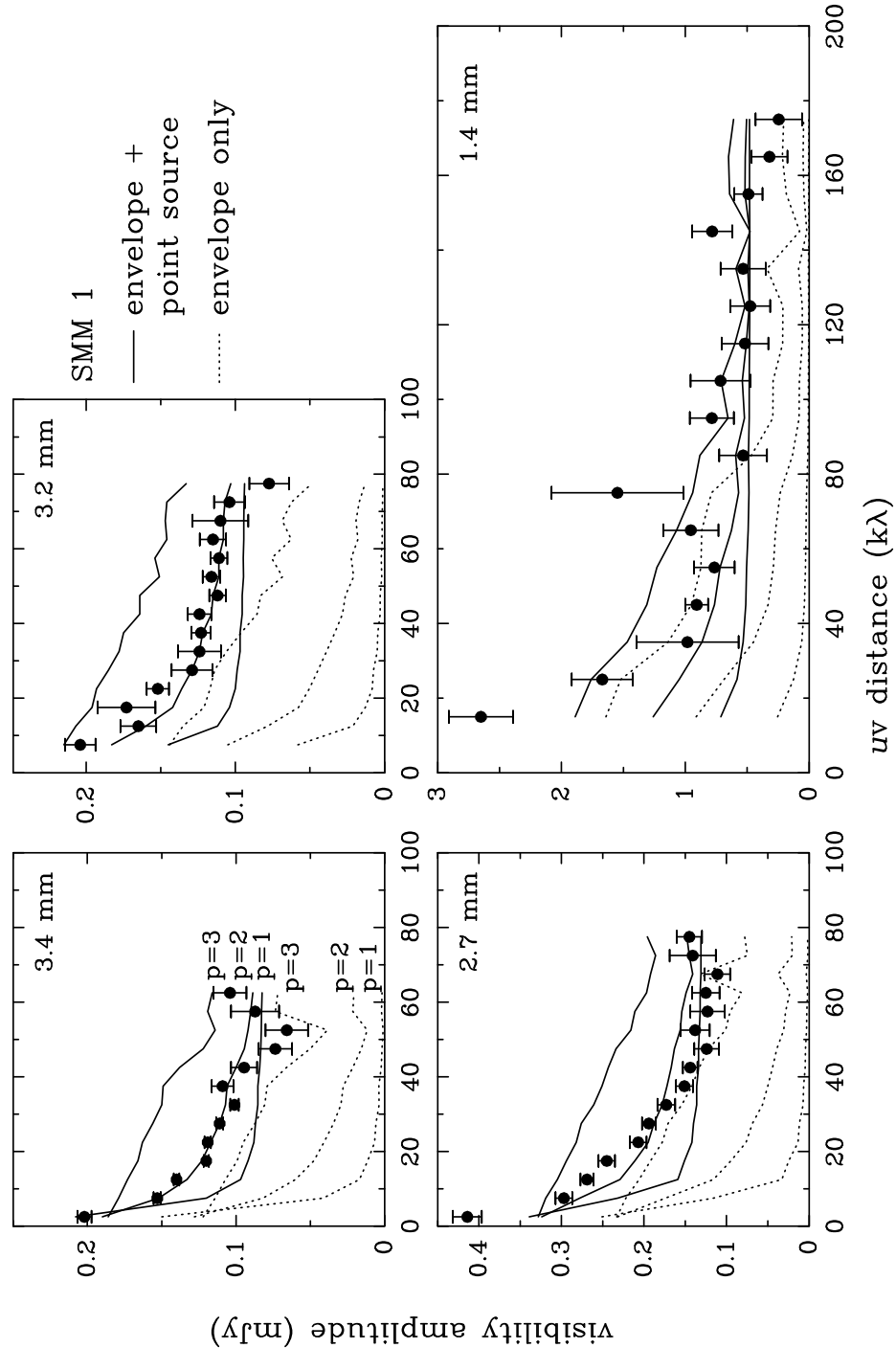


Fig. 4a

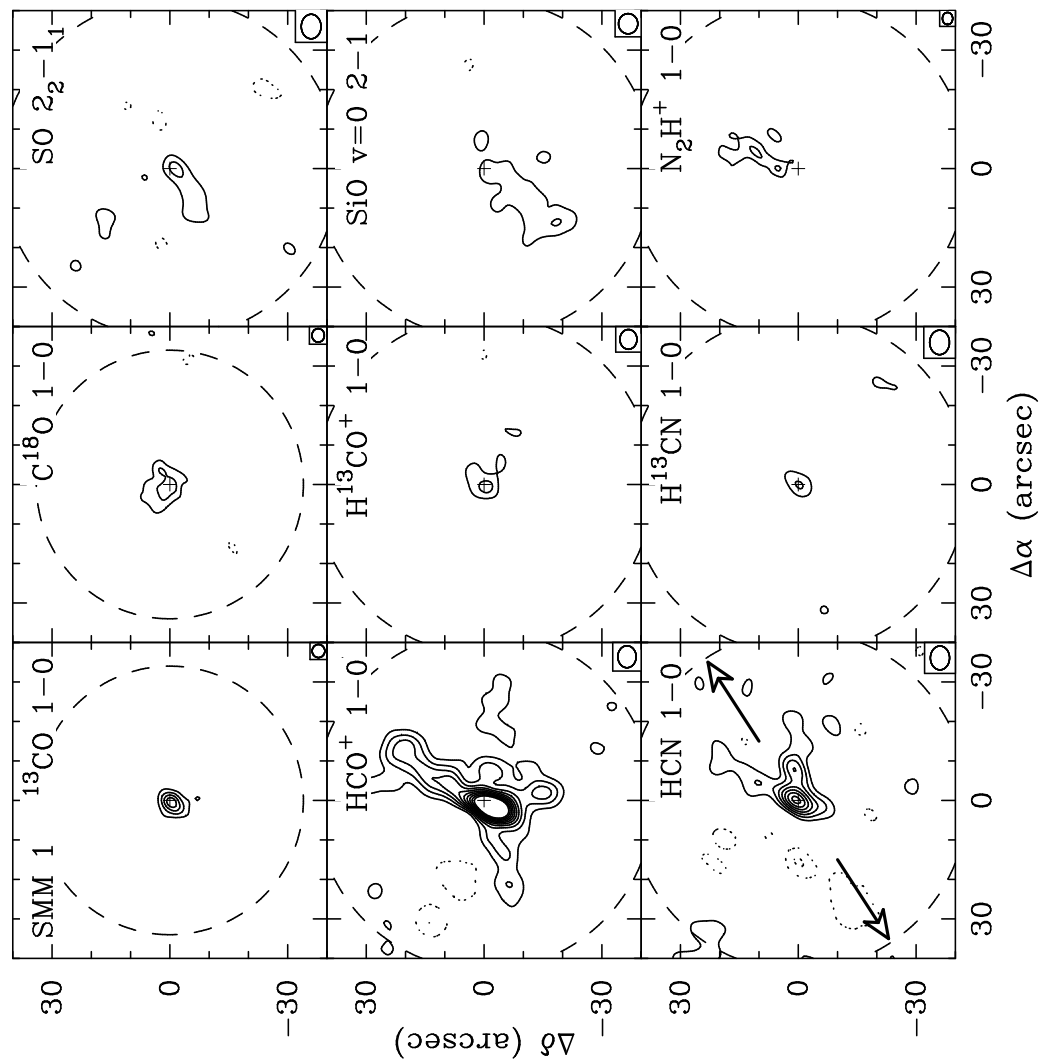


Fig. 4b

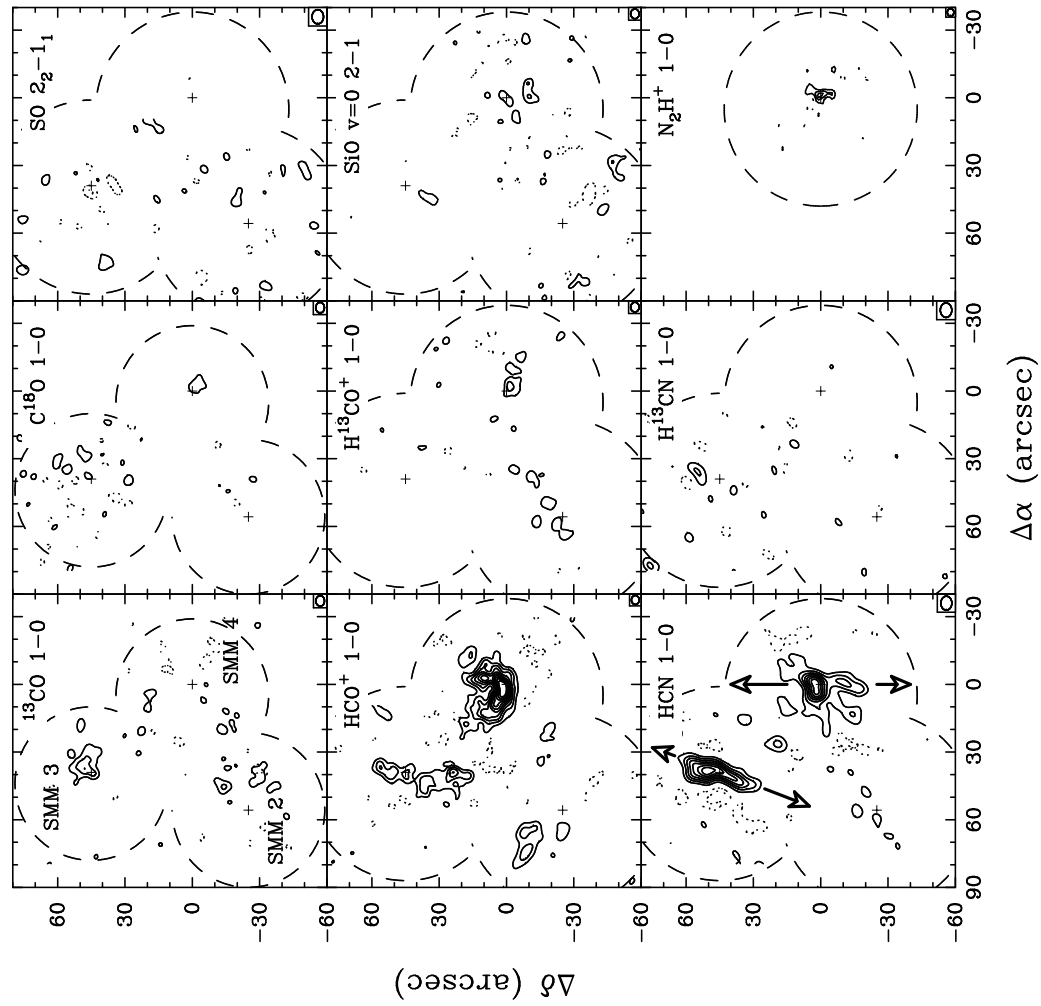


Fig. 5

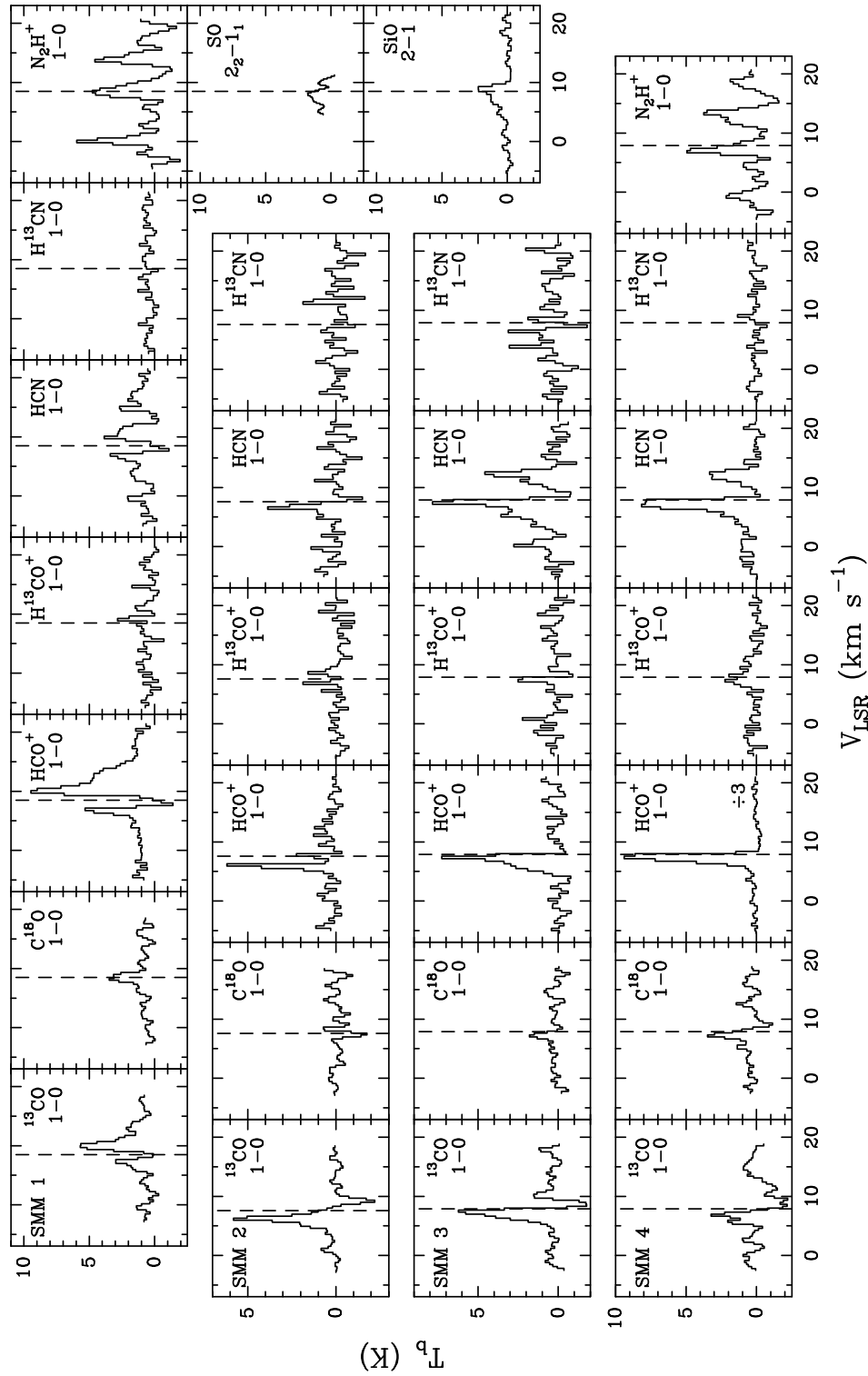


Fig. 6a

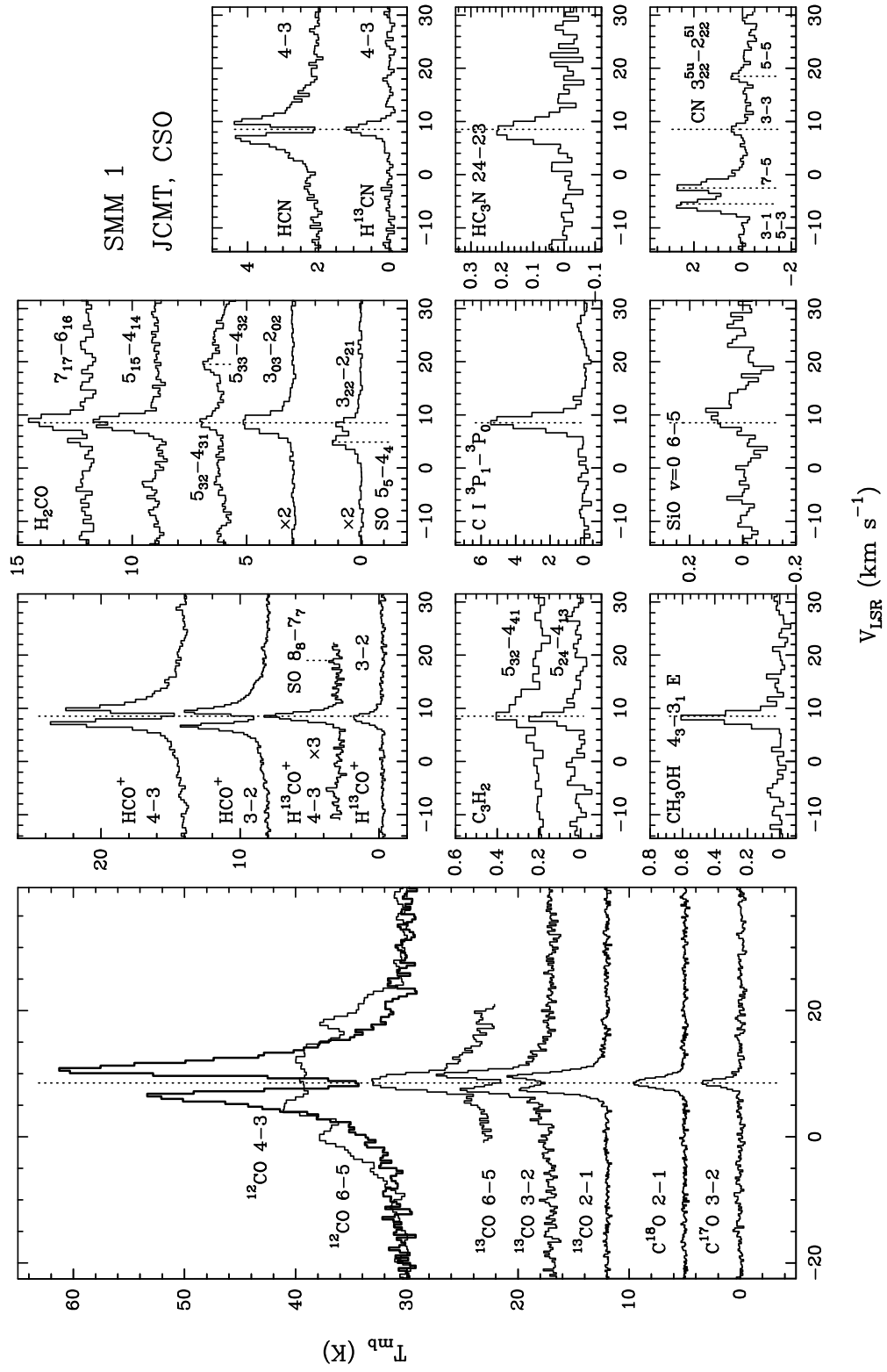


Fig. 6b

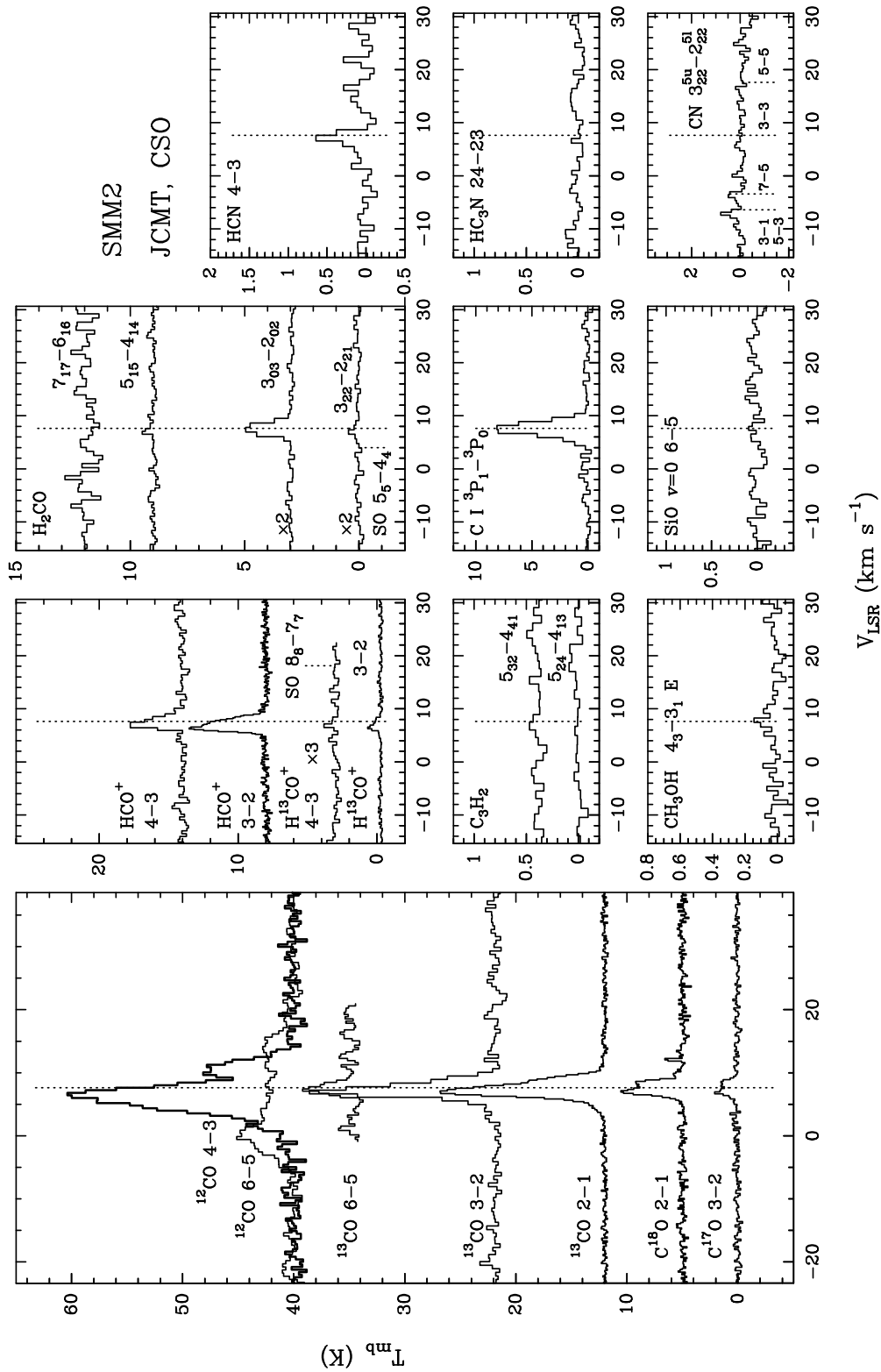


Fig. 6c

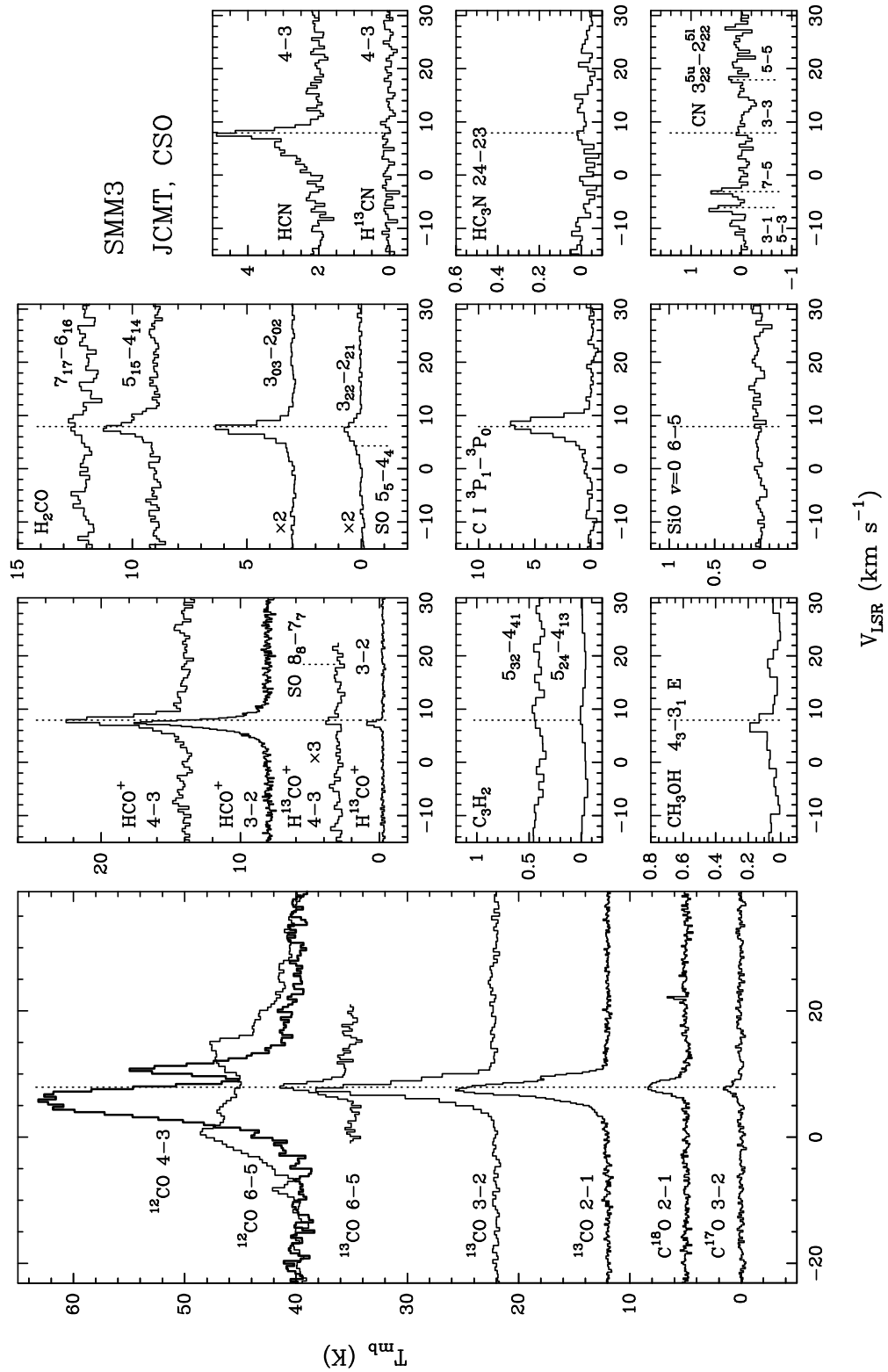


Fig. 6d

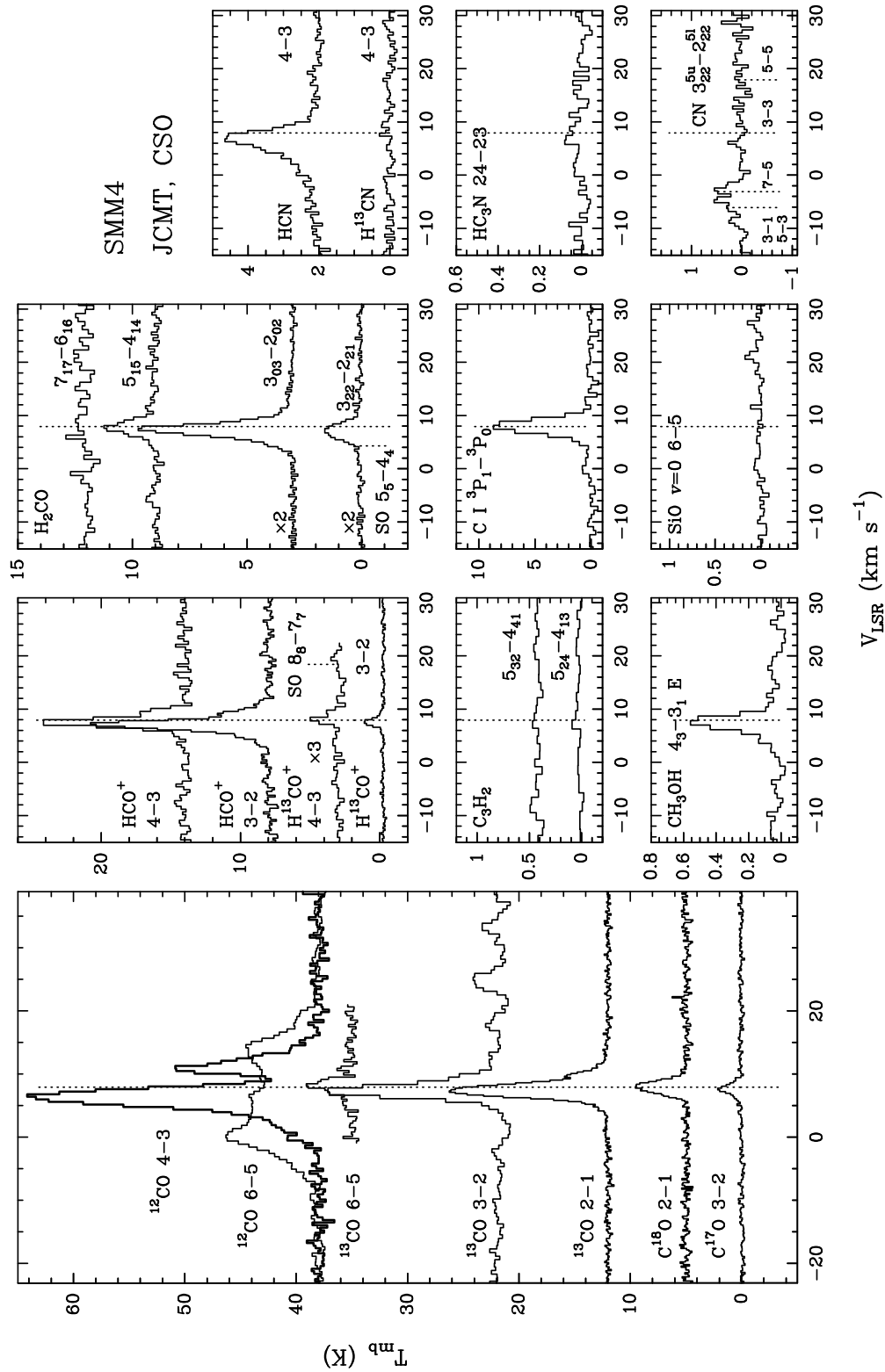


Fig. 7a

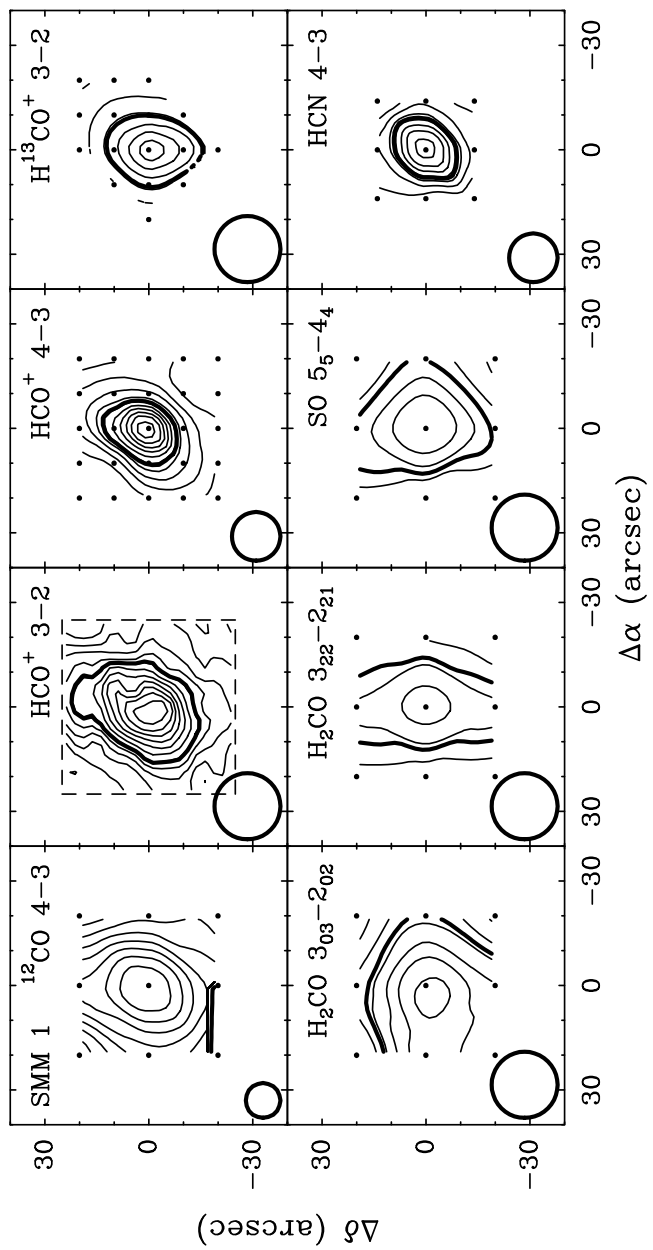


Fig. 7b

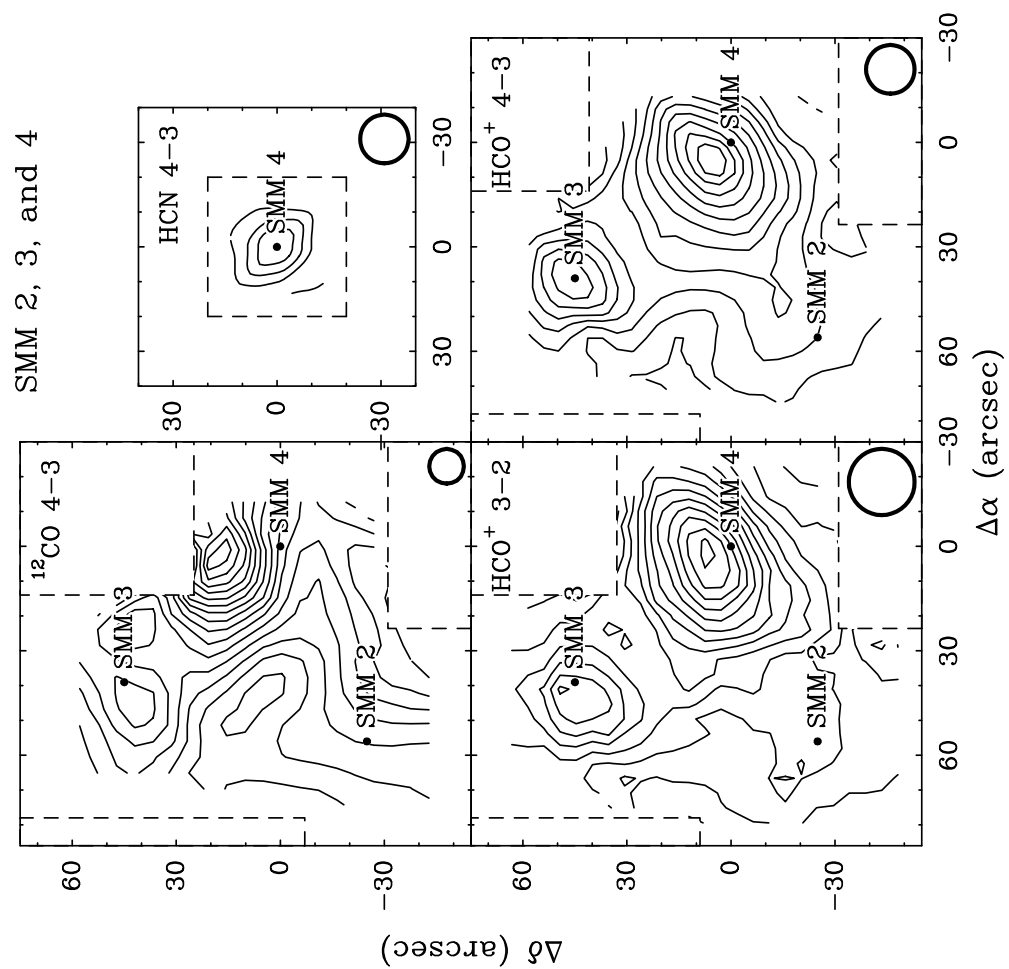


Table 1. Source sample

Source	α (1950.0) ^a (hh mm ss)	δ (1950.0) ^a ($^{\circ}$ ' '')	L_{bol} ^b (L_{\odot})	F_{ν} (1.1 mm) (Jy)	M_{\star} ^c (M_{\odot})
SMM 1 = FIRS 1	18 27 17.3	+01 13 16	77	3.47 ± 0.1	0.7–3.9
SMM 2	18 27 28.0 ^d	+01 10 45 ^d	10	0.6 ± 0.1	0.1–2.1
SMM 3	18 27 26.9	+01 11 55	13	1.11 ± 0.1	0.1–2.2
SMM 4	18 27 24.3	+01 11 10	15	1.47 ± 0.1	0.1–2.3

^aBest-fit positions to continuum interferometric data (see §4.1).

^bScaled to a distance of 400 pc.

^cConstraints on stellar mass derived from bolometric luminosity. Lower limit: L_{bol} due to accretion at $\dot{M} = 10^{-5} M_{\odot} \text{ yr}^{-1}$ onto star with $3 R_{\odot}$ radius. Upper limit: main-sequence mass of star with stellar luminosity equal to L_{bol} .

^dNo continuum emission detected in interferometer beam. Submillimeter position of Casali et al. (1993) is given.

References. — Casali et al. 1993 (F_{ν} 1.1 mm); Hurt & Barsony 1996 (L_{bol}).

Table 2. Overview of observations

Date	Instrument	Observation
Interferometer data		
1994 Oct–Dec, 1996 Feb–May, 1997 Feb–Apr	OVRO	$F_\nu(\lambda = 3.4 \text{ mm})$
1997 Apr	OVRO	$F_\nu(\lambda = 3.2 \text{ mm})^a$
1995 Feb, May, 1997 Feb–Mar	OVRO	$F_\nu(\lambda = 2.7 \text{ mm})$
1997 Feb–Mar	OVRO	$F_\nu(\lambda = 1.3 \text{ mm})^b$
1997 Apr	OVRO	$F_\nu(\lambda = 1.4 \text{ mm})^a$
1995 Feb, May, 1997 Feb–Apr	OVRO	$^{13}\text{CO } 1-0; \text{C}^{18}\text{O } 1-0$
1994 Oct–Dec	OVRO	$\text{HCO}^+ 1-0; \text{H}^{13}\text{CO}^+ 1-0; \text{SiO } 2-1$
1996 Feb–May, 1997 Feb–Apr	OVRO	$\text{HCN } 1-0; \text{H}^{13}\text{CN } 1-0; \text{C}_3\text{H}_2 4_{32}-4_{23}; \text{SO } 2_2-1_1$
1997 Apr	OVRO	$\text{N}_2\text{H}^+ 1-0^a; \text{C}^{34}\text{S } 2-1^a$
Single-dish data		
1995 May	CSO	$^{12}\text{CO } 6-5^d, ^{13}\text{CO } 6-5^d$
1995 Oct	CSO	$\text{H}^{13}\text{CO}^+ 4-3; \text{SO } 8_8-7_7$
1995 Mar, Jun	JCMT	$^{12}\text{CO } 4-3^e, ^{13}\text{CO } 2-1, 3-2; \text{C}^{18}\text{O } 2-1; \text{C}^{17}\text{O } 3-2; \text{SiO } 6-5;$ $\text{HCO}^+ 3-2^e, 4-3^e; \text{H}^{13}\text{CO}^+ 3-2^f; \text{HC}_3\text{N } 24-23^f; \text{SO } 55-44^{f,g};$ $\text{CN } 3\frac{5}{2}-2\frac{3}{2}\frac{1}{2}, 3\frac{5}{2}-2\frac{3}{2}\frac{3}{2}, 3\frac{5}{2}-2\frac{3}{2}\frac{5}{2}, 3\frac{5}{2}-2\frac{3}{2}\frac{3}{2}, 3\frac{5}{2}-2\frac{3}{2}\frac{5}{2};$ $\text{H}_2\text{CO } 7_{17}-6_{16}, 5_{15}-4_{14}, 5_{33}-4_{32}^c, 5_{32}-4_{31}^c, 3_{03}-2_{02}, 3_{22}-2_{21}^{f,g};$ $\text{C}_3\text{H}_2 5_{24}-4_{13}^f, 5_{32}-4_{41}; \text{CH}_3\text{OH } 4_{2}-3_1 \text{ E}^f; \text{C I } ^3\text{P}_1-^3\text{P}_0$
1996 Aug	JCMT	$\text{HCN } 4-3; \text{H}^{13}\text{CN } 4-3$

^aSMM 1 and SMM 4 only.

^bSMM 2 and SMM 3 only.

^cSMM 1 only.

^dFive-point map obtained.

^eMap obtained.

^fMap obtained of SMM 1 only.

^g $\text{H}_2\text{CO } 3_{22}-2_{21}$ and $\text{SO } 55-44$ are partially blended, in upper and lower sideband respectively.

Table 3. Millimeter-continuum data

Source	λ (mm)	beam ($''$)	$I(\text{max})$ (Jy beam $^{-1}$)	$F_\nu(\text{total})$ (Jy)
SMM 1	3.4	5.8×4.9	0.126	0.202
	3.2	2.4×1.5	0.122	0.204
	2.7	3.2×2.7	0.183	0.414
	1.4	1.1×0.7	0.615	2.650
SMM 2	3.4	5.3×5.0	< 0.005	...
	2.7	4.2×3.6	< 0.008	...
	1.4	2.4×1.5	< 0.11	...
SMM 3	3.4	5.2×4.4	0.043	0.052
	2.7	4.3×3.6	0.090	0.104
	1.4	2.4×1.5	0.651	0.900
SMM 4	3.4	5.3×4.6	0.060	0.075
	3.2	2.6×1.5	0.068	0.097
	2.7	3.2×2.7	0.092	0.143
	1.4	1.1×0.7	0.462	1.108

Table 4. Envelope model and best-fit parameters

	SMM 1	SMM 3	SMM 4
R_{in} (AU) ^a	100	100	100
R_{out} (AU) ^a	8000	8000	8000
Density: $\rho(r) = \rho_0(r/1000 \text{ AU})^{-p}$			
p	-2.0 ± 0.5	-2.0 ± 0.5	-2.0 ± 0.5
$M_{\text{env}}(M_\odot)$	8.7	3.0	5.3
Dust temperature: $T_{\text{dust}} = T_0(r/1000 \text{ AU})^{-0.4}$			
T_0	27 K	24 K	20 K
Point-source flux ^b			
$F_\nu(2.7 \text{ mm})$ (Jy)	0.13	0.05	0.07

^aFixed parameter.

^bAdditional unresolved component to fit flux on long baselines. See text.

Table 5. Overview of regions traced by the various observations presented in this paper

Component	Interferometer	Single dish
Bulk of the (cold) envelope	Continuum on short spacings	^{13}CO 2–1, 3–2; C^{18}O 2–1; C^{17}O 3–2 HCO^+ 3–2, 4–3 (line center); H^{13}CO^+ 3–2, 4–3 HCN 4–3 (line center); H^{13}CN 4–3 H_2CO 303–202, 515–414, 717–616 C_3H_2 532–441; HC_3N 24–23; CN 3 $\frac{5}{2}$ –2 $\frac{3}{2}$ SiO 6–5 ^a ; SO 55–44, 88–77 ^a
Inner regions of the envelope	Continuum on intermediate spacings ^{13}CO , C^{18}O 1–0 H^{13}CO^+ , H^{13}CN , N_2H^+ 1–0	...
Additional warm material ^b Bipolar outflow	Continuum on longest spacings SiO 2–1; SO 2 ₂ –1 ₁	^{12}CO 4–3, 6–5; ^{13}CO 6–5; H_2CO 322–221 ^{12}CO 4–3, 6–5 (wings); ^{13}CO 6–5 (wings) HCN 4–3 (wings)
Walls of the outflow cavity	HCO^+ 1–0; HCN 1–0	...
Surrounding quiescent cloud	C_3H_2 432–423 (clumps)	[C I] $^3\text{P}_1$ – $^3\text{P}_0$ (surface)

^aFor the observations of SMM 1 do the single-dish SiO and SO observations trace the envelope only, because the beam did not cover the SiO and SO peak due to the outflow seen in the OVRO images.

^bAssociated with the innermost few hundred AU of the envelopes, where the temperature exceeds the adopted $T_{\text{kin}} \propto r^{-0.4}$ relation (see text).

Table 6. OVRO integrated intensities and line opacities

Source	Line	$5'' \times 5''$ area		$20'' \times 20''$ area	
		$\int T_b dV$ (K km s $^{-1}$)	$\bar{\tau}$	$\int T_b dV$ (K km s $^{-1}$)	$\bar{\tau}$
SMM 1	^{13}CO 1–0	27.1 ± 0.3	2.1	2.49 ± 0.08	6.5
	C^{18}O 1–0	7.4 ± 0.1	0.3	1.38 ± 0.03	0.8
	C^{34}S 2–1	< 3.9	...	< 1.0	...
	C_3H_2 4 ₃₂ –4 ₂₃	2.0 ± 0.1	...	0.34 ± 0.02	...
	HCO^+ 1–0	48.4 ± 0.1	19.5	14.0 ± 0.03	7.7
	H^{13}CO^+ 1–0	12.5 ± 0.2	0.3	1.56 ± 0.06	0.1
	HCN 1–0	22.0 ± 0.1	15.5	4.96 ± 0.03	5.3
	H^{13}CN 1–0	4.7 ± 0.1	0.2	0.39 ± 0.03	0.1
	N_2H^+ 1–0	1.4 ± 0.1	...	3.79 ± 0.22	2 ± 1
	SiO 2–1	3.9 ± 0.1	...	1.62 ± 0.03	...
	SO 2 ₂ –1 ₁	2.0 ± 0.1	...	0.43 ± 0.01	...
	^{13}CO 1–0	< 0.5	...	0.25 ± 0.05	< 5.5
SMM 2	C^{18}O 1–0	< 0.3	...	< 0.1	< 0.7
	C_3H_2 4 ₃₂ –4 ₂₃	< 0.4	...	< 0.10	...
	HCO^+ 1–0	< 0.5	...	0.64 ± 0.04	...
	H^{13}CO^+ 1–0	1.2 ± 0.1	...	1.23 ± 0.03	...
	HCN 1–0	1.2 ± 0.2	...	1.53 ± 0.04	5 ± 4
	H^{13}CN 1–0	< 0.8	...	< 0.2	< 0.1
	SiO 2–1	< 1.3	...	< 0.3	...
	SO 2 ₂ –1 ₁	< 0.5	...	< 0.1	...
	^{13}CO 1–0	11.8 ± 0.2	< 5.5	3.37 ± 0.05	< 0.2
	C^{18}O 1–0	< 0.45	< 0.7	< 0.15	< 0.1
	C_3H_2 4 ₃₂ –4 ₂₃	< 0.33	...	< 0.12	...
	HCO^+ 1–0	9.3 ± 0.2	< 2.4	4.07 ± 0.05	< 1.1
SMM 3	H^{13}CO^+ 1–0	< 0.36	< 0.04	< 0.1	< 0.1
	HCN 1–0	33.2 ± 0.2	< 0.5	12.8 ± 0.06	2.8
	H^{13}CN 1–0	< 0.9	< 0.1	0.7 ± 0.1	3.5
	SiO 2–1	< 1.8	...	< 0.51	...
	SO 2 ₂ –1 ₁	< 0.4	...	< 0.1	...
	^{13}CO 1–0	< 0.75	...	< 0.21	...
	C^{18}O 1–0	4.4 ± 0.1	...	0.82 ± 0.02	...
	C^{34}S 2–1	< 5.0	...	< 1.5	...
	C_3H_2 4 ₃₂ –4 ₂₃	0.5 ± 0.1	...	< 0.06	...
	HCO^+ 1–0	40.8 ± 0.2	9.3	18.0 ± 0.06	4.2
	H^{13}CO^+ 1–0	5.4 ± 0.1	0.1	1.13 ± 0.04	< 0.1
	HCN 1–0	31.4 ± 0.2	< 0.5	13.3 ± 0.04	< 0.2
SMM 4	H^{13}CN 1–0	< 0.6	< 0.1	< 0.15	< 0.1
	N_2H^+ 1–0	7.8 ± 1.2	< 2.0	< 1.0	...
	SiO 2–1	< 1.2	...	0.28 ± 0.11	...
	SO 2 ₂ –1 ₁	< 0.3	...	< 0.06	...

Table 7. Single-dish integrated line intensities and opacities

Line	SMM 1		SMM 2		SMM 3		SMM 4	
	$\int T_{\text{mb}} dV^{\text{a}}$ (K km s ⁻¹)	$\bar{\tau}^{\text{b}}$	$\int T_{\text{mb}} dV^{\text{a}}$ (K km s ⁻¹)	$\bar{\tau}^{\text{b}}$	$\int T_{\text{mb}} dV^{\text{a}}$ (K km s ⁻¹)	$\bar{\tau}^{\text{b}}$	$\int T_{\text{mb}} dV^{\text{a}}$ (K km s ⁻¹)	$\bar{\tau}^{\text{b}}$
¹² CO 4–3	232.2 ± 2.2	...	120.6 ± 1.7	...	171.3 ± 1.8	...	148.5 ± 1.6	...
6–5	221.9 ± 2.7	13.5	60.1 ± 1.8	6.4	165.7 ± 2.0	5.2	134.5 ± 1.4	4.6
¹³ CO 2–1	27.0 ± 0.2	3.4	40.8 ± 0.3	5.5	43.1 ± 0.3	0.9	42.8 ± 0.3	2.0
3–2	35.8 ± 0.6	7.3	39.9 ± 0.8	5.5	50.1 ± 0.6	2.4	45.7 ± 0.7	4.0
6–5	41.4 ± 1.0	0.2	5.6 ± 0.7	0.1	12.8 ± 0.6	0.1	9.2 ± 0.5	0.1
C ¹⁸ O 2–1	9.5 ± 0.2	0.4	13.0 ± 0.3	0.3	7.7 ± 0.3	0.1	11.0 ± 0.3	0.3
C ¹⁷ O 3–2	5.7 ± 0.3	0.2	4.9 ± 0.2	0.1	3.0 ± 0.2	0.1	4.2 ± 0.2	0.1
HCO ⁺ 3–2	33.3 ± 0.4	12.4	13.1 ± 0.2	9.1	21.8 ± 0.3	5 ± 3	36.0 ± 0.5	5.5
4–3	48.1 ± 0.7	4.3	8.8 ± 0.5	< 3.1	20.4 ± 0.8	< 0.2	25.0 ± 0.6	3.0
H ¹³ CO ⁺ 3–2	5.8 ± 0.2	0.2	1.7 ± 0.1	0.1	1.6 ± 0.8	0.1	2.9 ± 0.1	0.1
4–3	3.1 ± 0.1	0.1	< 0.4	< 0.1	0.2 ± 0.1	< 0.1	1.2 ± 0.1	0.1
HCN 4–3	17.5 ± 0.4	12.3	1.4 ± 0.3	...	10.1 ± 0.3	< 0.2	14.0 ± 0.4	< 2.1
H ¹³ CN 4–3	3.0 ± 0.2	0.2	< 0.8	< 0.1	< 0.5	< 0.1
H ₂ CO 3 ₀₃ –2 ₀₂	4.6 ± 0.1	...	2.7 ± 0.1	...	4.9 ± 0.1	...	11.0 ± 0.1	...
3 ₂₂ –2 ₂₁ ^d	1.8 ± 0.1	...	0.4 ± 0.1	...	1.7 ± 0.1	...	2.93 ± 0.1	...
5 ₁₅ –4 ₁₄	8.0 ± 0.3	...	0.7 ± 0.2	...	7.2 ± 0.3	...	6.4 ± 0.3	...
5 ₃₂ –4 ₃₁	3.3 ± 0.3
5 ₃₃ –4 ₃₂	2.8 ± 0.3
7 ₁₇ –6 ₁₆	6.7 ± 0.6	...	< 1.5	...	< 1.3	...	< 1.6	...
C I ³ P ₁ – ³ P ₀	18.0 ± 0.7	...	26.7 ± 1.0	...	30.3 ± 1.0	...	29.8 ± 0.9	...
C ₃ H ₂ 5 ₂₄ –4 ₁₃	0.7 ± 0.1	...	< 0.3	...	< 0.2	...	< 0.2	...
5 ₃₂ –4 ₄₁	1.0 ± 0.1	...	< 0.3	...	< 0.2	...	< 0.3	...
CH ₃ OH 4 ₂ –3 ₁ E	1.4 ± 0.1	...	< 0.3	...	0.6 ± 0.1	...	2.1 ± 0.1	...
HC ₃ N 24–23	0.9 ± 0.1	...	< 0.5	...	< 0.2	...	< 0.2	...
CN 3 ₂ ⁵ ₃ –2 ₂ ³ ₁ , 3 ₂ ₂ –2 ₂ ₂ ^c	6.6 ± 0.3	...	1.4 ± 0.2	...	0.7 ± 0.2	...	1.4 ± 0.2	...
3 ₂ ₂ –2 ₂ ₁ ^c	0.8 ± 0.2	...	< 0.6	...	< 0.6	...	< 0.5	...
3 ₂ ₂ –2 ₂ ₂ ^c	< 0.8	...	< 0.6	...	< 0.6	...	< 0.5	...
3 ₂ ₂ –2 ₂ ₂ ^c	6.0 ± 0.2	...	< 0.6	...	0.6 ± 0.2	...	0.8 ± 0.2	...
SO 5 ₅ –4 ₄ ^d	1.4 ± 0.1	...	< 0.3	...	< 0.1	...	< 0.2	...
8 ₈ –7 ₇	0.3 ± 0.1	...	< 0.3	...	0.3 ± 0.1	...	< 0.3	...
SiO 6–5	0.5 ± 0.1	...	< 0.3	...	< 0.2	...	< 0.3	...

^aUpper limits are 3 σ .

^bUsing abundance ratios [¹²C] : [¹³C] = 65 : 1 and [¹⁶O] : [¹⁸O] : [¹⁷O] = 2695 : 5 : 1.

^cCN 3₂₂⁵₃–2₂₂³₁ and 3₂₂⁵₅–2₂₂³₃ are partially blended with 3₂₂⁷₇–2₂₂⁵₅. Assuming equal contributions to integrated intensity.

^dH₂CO 3₂₂–2₂₁ and SO 5₅–4₄ are partially blended. Assuming equal contributions for SMM 1, and no contribution from SO for SMM 2, 3, and 4 (cf. spectra in Fig. 6).

Table 8. Derived molecular abundances

Species	Envelope			Warm gas ^a			
	SMM 1	SMM 3	SMM 4	SMM 1	SMM 3	SMM 4	IRAS 16293–2422 ^b
¹² CO ^c	≡ 1(–4)	≡ 1(–4)	≡ 1(–4)	≡ 1(–4)	≡ 1(–4)	≡ 1(–4)	...
HCO ⁺	1(–9)	1(–9)	1(–9)	2(–8)	2(–8)	1(–7)	2(–9)
HCN	2(–9)	2(–9)	2(–9)	5(–8)	1(–7)	8(–8)	2(–9)
H ₂ CO	8(–10)	2(–9)	2(–9)	9(–9)	2(–8)	1(–7)	7(–10)
C ₃ H ₂	2(–10)	< 3(–10)	< 3(–10)	3(–9)	< 3(–9)	< 7(–9)	4(–11)
CN	5(–9)	2(–10)	2(–10)	3(–8)	1(–8)	1(–7)	1(–10)
HC ₃ N	2(–10)	< 2(–10)	< 2(–10)	9(–10)	< 4(–9)	< 6(–9)	3(–11)
SiO	1(–11)	< 2(–11)	< 2(–11)	1(–10)	< 4(–10)	< 1(–9)	1(–10)
SO	2(–10)	< 1(–10)	< 2(–10)	2(–9)	< 2(–9)	< 7(–9)	4(–9)
C I ^d	9(–6)	5(–5)	3(–5)	4(–5)	3(–4)	8(–4)	...

^aAbundances derived under the assumption that all emission except CO originates in the additional column of ~ 100 K gas. See text.

^bAverage abundances in a 20'' beam toward the class 0 YSO IRAS 16293–2422, for comparison (van Dishoeck et al. 1995).

^cAbundance of CO is fixed, except for depletion. See text.

^dDerived abundance of C I is highly uncertain, because the low-density surface of the entire Serpens Molecular Cloud is likely to contribute significantly to the emission in the $^3\text{P}_1 - ^3\text{P}_0$ line.